A Large Acceptance Experiment at The CERN Super Proton Synchrotron to study elastic and other 2-body hadronic interactions up to 100 GeV/c.

L. Bugge and T. Buran

Report 80-07

A Large Acceptance Experiment at The CERN Super Proton Synchrotron to study elastic and other 2-body hadronic interactions up to 100 GeV/c.

L. Bugge and T. Buran

Abstract

In this report we describe an experiment at The CERN Super Proton Synchroton to measure elastic scattering between hadrons [1]. The equipment, the trigger logic and the data analysis is described in some detail.

The data have so far been obtained at 20 GeV/c, 30 GeV/c and 50 GeV/c primary beam momentum.

The acceptance of the apparatus covers the c.m. scattering angular range from about 10^{o} to about 100^{o}.

The results, which are preliminary, are presented with some accompanying comments. The Constituent Interchange Model is compared to the results at the wider angles in the c.m. system. The model disagrees with the results. However, the scaling law which follows from dimensional considerations assuming that quark dynamics are the fundamental interactions, is consistent with our results in the large c.m. scattering angle region.

The $\bar{p}p$ elastic scattering cross section has been measured in the region $1(\mathrm{GeV/c})^2 \leq -t \leq 3.5\ (\mathrm{GeV/c})^2$ at 50 GeV/c.

A dip is observed at $-t \simeq 1.4\ (\mathrm{GeV/c})^2$. The differential cross section coincides with the pp elastic differential cross section at 1500 GeV/c. (See footnote p. 24).

CONTENTS

INTRODUCTION

The quark-parton model is believed to be the correct description of deep inelastic lepton hadron and hadron-hadron interactions at high energies where short distance behaviour plays an important role.

In its semiclassical approximation it gives a qualitative and an approximate quantitative description of lepton pair production, single particle production and jet production at high transverse momentum.

While in lepton hadron scattering experiments the hadron structure has been studied it is only in hadron hadron scattering that parton parton interactions are believed to be the underlying dynamics.

In lepton hadron scattering the scaling functions are known. As we do not have a clear description of parton parton scattering the high transverse momentum hadron hadron interactions are less well understood.

Inelastic hadron hadron collisions are described in various models for quark interactions. The interpretations are beset with uncertainties due to the fragmentation functions, to the transverse momenta of the constituents of the hadrons, giving rise to trigger bias effects, and to unknown perturbation effects expected from the quantum chromodynamic field theory.

Elastic high transverse momentum hadron hadron collisions at high energies are also believed to be dominated by quark dynamics. The models for the constituent interactions are put to a more stringent test than in the inelastic case. Trigger bias effects and the poorly known fragmentation functions do not enter.

Experimentally it is very difficult to measure elastic scattering cross sections at high transverse momenta at high energies. One has to manage high intensity beams and to have a high rejection of the dominating background. We have aimed at measuring these cross sections down to 10^{-38} cm^2.

To do this we had to design and build apparatus with a much higher precision and sensitivity than had been done up to then.

Besides the results at high transverse momenta we have also studied the cross sections in the region where the parton model gradually develops into the Regge model. That is at smaller four momentum transfers, however not in the very forward direction.

The experiment is done in the West Hall at The Super Proton Synchroton at CERN. Data have been collected at 20 GeV/c, 30 GeV/c and 50 GeV/c primary beam momenta, with both positive and negative beams.

The first part of this report is a description of the experimental equipment, the trigger logic and the data analysis. The results obtained so far are contained in the second part. The results are preliminary.

The experiment is a collaboration work between the following laboratories, CERN, LAPP (L'aboratoire d'Annecy de Physique des particules), Niels Bohr Institute in Copenhagen, University of Genova, University College in London and University of Oslo.

1. THE EXPERIMENTAL TECHNIQUE

1. Experimental Lay-Out

The location of the experiment in the CERN West Hall is shown in fig. 1. Two basically different set-ups have been used so far. The one shown in fig. 2 is used for measurements of the reactions at the highest momentum transfers (high-t set-up). The other one, sketched in fig. 3, is used for measurements of the reactions at somewhat lower momentum transfers (medium-t set-up).

The left (viewed downstream) arm is essentially the same in the two set-ups. This arm will also be referred to as the forward arm, since the trigger (see sect. 7) only accepts elastic events with the recoil proton in the right arm. Accordingly the right arm will also be referred to as the recoil arm.

In the medium-t set-up the target is moved ~3 m further upstream and the experiment is equipped with a new right arm upstream of the magnet.

The codes on figs. 2 and 3 will be explained in the subsequent sections.

2. The Beam and Beam Particle Detection

The target T3 (fig. 1) is struck by protons from the SPS of maximum 250 GeV/c momentum. The secondary beam follows a beam line which has two branches, the E1A/H1A beam line to Omega and the E1B/H1B beam line to WA7.

The distance from T3 to WA7 is about 182 m. The angular acceptance of the E1B/H1B beam is ±1.2 mrad in x and ±2.8 mrad in y.

The maximum beam momentum is 100 GeV/c with a resolution of $\frac{\Delta p}{p} \sim 2\%$.

The beam cross sectional area at the WA7 target is about 5 by 2.5 cm^2.

The beam optics is shown in fig. 4. It consists of a system of dipole bending magnets (BEND,TR), quadrupole magnets for beam focusing (Q) and collimators (CH,CV) for spatial definition of the beam.

Beam monitoring devices are four multiwire proportional chamber planes (dotted lines in fig. 4), scintillation counters, an ionization chamber, and three differential Cerenkov counters (CEDARs, short for CErenkov Differential counters with Acromatic Ring focus [2]). Two of the CEDARs are located upstream of the experiment, and one downstream. At medium-t data-taking one of the upstream CEDARs is removed.

In the high-t set-up four scintillation counters are mounted around the beam upstream of the target. They count the halo and constitute the beam veto counters. In the medium-t set-up the beam veto is given by three counters immediately downstream of the target. During medium-t data-taking there is in addition placed a large area veto counter between the upstream edge of the target and the right (viewed into the recoil arm from target) edge of H3 (see fig. 3).

The beam is unseparated and contains π, K, p, e and μ. Fig. 5 shows the calculated particle intensities normalized to 10^{12} interacting protons in T3, as functions of the beam momentum.

Measurements showed that the hadron intensities of fig. 5 are too high by a factor 5, whereas the calculated electron intensity is too low.

The beam particle identification is given by the CEDARs. During high-t data-taking they are set to count p, K and K, respectively.

The reason for the third CEDAR downstream of the experiment is as follows. At the highest intensities there is a finite probability that a π accompanies a K inside the CEDAR resolution time. If then the π scatters, the event might be misidentified as a Kp event since the threshold Cerenkovs C1 and C2 (see section 4.1) cannot distinguish effectively between π and K. This possibility of misidentification is ruled out when a third CEDAR counts unscattered K-mesons.

Fig. 6 shows a scan of one of the CEDARs (i.e. counts as a function of CEDAR pressure) at 20 GeV/c negative beam. It shows the ratios

$\pi^-/K^-/\bar{p} \approx 0.900/0.030/0.028$

The μ contamination of the beam is difficult to measure in the same way because of the divergence of the decay product μ's. It is estimated, however, to be of the order of 6% at 20 GeV/c.

To minimize the electron contamination a piece of lead, 4.6 mm thick, is located in the beam, reducing the electron content to effectively zero.

The position and direction of the beam trigger particle is determined by means of the two beam hodoscopes. They are located about 1 and 8 meters upstream of the target (high-t set-up), respectively.

Each hodoscope consists of 3 planes. One plane is constructed from two rows of 20 scintillators each, arranged as shown in fig. 7. The scintillator elements have dimensions $100\times5\times2.2\ mm^3$. Each one is viewed by a photo multiplier through a light guide. The three planes of a hodoscope are mounted with the scintillators vertical and at ±45 degrees, respectively.

In the medium-t set-up the downstream beam-hodoscope and CEDAR2 (fig. 4) are removed. Instead of CEDAR2 a 4 m long atmospheric pressure threshold Cerenkov, CP1 (fig. 3), is placed in the beam immediately upstream of the target. This counter (set to count π) is optimized to manage rates up to $\sim5\times10^7$/s [3].

To measure the beam flux, an ionization chamber is installed upstream of CEDAR1.

3. Target and Spectrometer Magnet

The target is a 1 m long mylar cylinder of 4 cm radius, filled with liquid H_2 at atmospheric pressure. In the high-t set-up it extends partly inside the magnetic field volume. In the medium-t set-up, it is pushed about 3 m further upstream, and surrounded by a target veto counter to reject inelastic reactions. This veto counter is only open in both ends of the target and along the right (viewed downstream) side to let the recoil proton into the recoil arm.

The spectrometer magnet has a volume of about $1.50 \times 0.75 \times 1.92\ m^3$. At the maximum current of 7500 A, the vertical, main component of the field reaches about 16 kG. The corresponding field integral is about 23 kGm.

Besides momentum analyzing the tracks (with a resolution of $\Delta p/p = 0.3\%\ p$ (in GeV/c)), the magnet effectively sweeps away low-momentum background.

The vertical inner walls of the magnet are covered with scintillation counters to reject inelastic events. They constitute the magnet veto counters.

4. The Detection of the Outgoing Particles

4.1 The Threshold Cerenkov Counters

The reaction products are identified by means of threshold Cerenkov counters. The left arm (fast particle) is provided with two Cerenkovs (C1 and C2) in both the high- and medium-t set-ups.

In the high-t set-up the recoil particle goes through the two Cerenkovs C3 and C4, whereas in the medium-t set-up it traverses the aerogel Cerenkov counter AC (fig. 3).

AC is a Cerenkov counter of $28 \times 80\ cm^2$ area. The Cerenkov light is produced in 9 cm of aerogel with a refractive index of about 1.03. This makes possible a distinction between π and p in the region of 4-momentum transfer between 1 and 6 GeV^2/c^2 [4].

The counters C1, C2, C3 and C4 are filled with gases at atmospheric pressure. The choice of gases depends on the beam momentum.

Table 1 summarizes the properties of the four threshold Cerenkovs used in the high-t set-up. The fillings refer to 20 GeV/c beam momentum.

Together with the CEDAR information, the threshold Cerenkov information uniquely identifies the events as $\pi p \to \pi p$, $Kp \to Kp$, or $pp \to pp$.

(It should be noted that for meson-proton events, the trigger only accepts the meson in the left and the proton in the right arm).

4.2 The Multi Wire Proportional Chambers

Accurate position measurements are provided by multiwire proportional chambers (MWPCs). In the high-t set-up the recoil arm is equipped with 4 chambers, CH1, CH2, CH3, and CH6 (fig. 2). In the medium-t set-up the 4 chambers CH7, CH8, CH9, and CH10 are used to reconstruct the recoil track (fig. 3).

The foreward arm is equipped with the 5 chambers CH1, CH2, CH3, CH4, and CH5 (fig. 2). At medium-t data-taking it is in addition provided with a sixth chamber, CH0, in front of the magnet (fig. 3).

Table 2 summarizes the properties of the different chambers. The coordinate projections are defined in fig. 8.

In the chambers CH0 - CH3 a mixture of Argon (~81.4%), Isobutane (~15%), Freon13B1 (~0.6%), and Methylalcohol (~3%) is used.

The large chambers CH4, CH5, and CH6 have a slightly different gas mixture, consisting of Argon (~75%), CO_2 (~24.5%) and Freon13B1 (~0.5%).

4.3 The Trigger Scintillation Counters

For triggering purposes rough position measurements with good time resolution are needed. This is achieved by means of hodoscopes of scintillation counter elements.

For the high-t trigger the H1, H2, PH1 and PH2 hodoscopes (fig. 2) are used.

In the medium-t set-up the H2 and PH2 hodoscopes are replaced by H3 and PH3 (fig. 3).

The H1, H2 and H3 hodoscopes consist of scintillation counter elements, each viewed by a photo multiplier through a solid light guide.

H1 and H2 each consists of two layers of 1 cm thick scintillators. In one layer the elements are ring-shaped, and in the other one they are wedgeshaped, as shown in fig. 9.

H1 has 14 rings each 5 cm wide, and H2 13 rings 8 cm wide. Both have 10 wedges of 15 degrees opening angle.

The polar coordinate structure of H1 and H2 facilitates the trigger logic which uses the kinematical constraints on coplanarity and opening angle of an elastic event.

H3 consists of 8 rectangular elements of size 30×12.1 cm^2. An exception is element no 2 (fig. 9) which is only 5 cm. wide. This is due to the mechanical support of the aerogel Cerenkov counter.

4.3.1 The Prompt Hodoscopes

In a high beam intensity, large acceptance experiment as WA7, it is essential to obtain good left-right time resolution in order to reduce the accidental trigger rate.

This is achieved by the so called prompt hodoscopes [5] which we will describe in some detail.

The left arm prompt hodoscope is PH1. The recoil arm prompt hodoscope is PH2 (high-t) or PH3 (medium-t). See figs. 2 and 3.

The prompt hodoscopes are built up from elements of three different sizes, 30×30 cm^2, 30×15 cm^2 and 15×15 cm^2, arranged in "rings" as shown in fig. 10.

Behind (i.e. downstream of) each scintillator element is mounted a photo multiplier. No solid light guide is used, as shown in fig. 11. The photo multiplier is placed on the axis of the element.

The scintillator and the photo multiplier are mounted in a black plastic box, as shown in fig. 12. The outside of the scintillator is covered by a sheet of aluminium foil to increase the light collection factor. The inside is roughened with emery paper to reduce the reflection of photons.

To reduce the time jitter, no light reflector is used on the inner wails of the black box. The time jitter then basically comes from two sources:

(i) The difference in path length for the photons and the difference in solid angle through which the impact point is seen by the photo multiplier for different impact positions.

(ii) The statistical fluctuations in the number of photo electrons which is small because of the restricted solid angle.

In order to obtain enough photo electrons, the scintillators are as thick as 4 cm.

With special discriminators [5] a time resolution of 0.52 ns is obtained, whereas it is 1.21 ns when ordinary electronics is used.

The structure of the prompt hodoscopes makes them well adapted to a system of fast coincidence matrices for rapid event evaluation in the trigger system.

5. The Iron Calorimeters

In the high-t arrangement each arm is provided with a rough calorimeter. The calorimeters consist of iron plates of dimension 200×200×10 cm^3, interspaced with scintillation counter planes as shown in fig. 13. The figure also shows the structure of a scintillator plane.

In the medium-t set-up only the foreward arm is equipped with a calorimeter.

At 30 GeV/c high-t data taking the two calorimeters were used in the trigger, reducing the trigger rate by about a factor 2.

At the time of writing, the fast arm calorimeter is being improved by increasing the number of scintillator planes. This will largely improve the medium-t trigger.

6. The Hardwired Processor

The hardwired processor is used as the third level in the high-t trigger (see the next section). It is divided into three parts:

(i) The Pre-Processor, which contains all necessary logic for interface with the data acquisition system. It reads multiwire proportional chamber information from the RMH (Receive Memory Hybrid) modules.

(ii) The Point Finder, which reconstructs 4- or 3-plane points in the chambers CH3, CH4 and CH6 (fig. 2).

(iii) The Coplanarity and Opening Angle tester, which makes accurate tests on opening angle and coplanarity of the straight lines reconstructed from the points found by the point finder.

The processor communicates with the NORD10 on-line computer to signal an accepted event.

Typically the non-destructive read-out uses ~100 ns per word. With typically 50 chamber words this gives a read-out time of ~5 μs. The average processing time per trigger is ~150 μs [6].

7. Trigger Logic and Data Acquisition

The trigger logic (high-t, but without the processor) is indicated in fig. 14. It is divided into three levels in order to minimize the dead time (only two levels are shown in fig. 14 since the processor is left out).

The first level is a rough test on the event geometry. By means of fast matrix logic (OR1-OR2, FM1-FM4), groups of elements in the hodoscopes and the prompt hodoscopes are correlated. In addition the beam- and magnet-veto counters enter.

The first level generates the fast strobe, which opens the registers and enables the RMH-modules for storing of MWPC-data.

A strobe inhibit flip-flop inhibits the formation of a new strobe for ~250 ns. This is the time level 2 of the trigger needs to arrive at a conclusion.

The second level performs a more accurate test on the event geometry by correlating the prompt hodoscopes on an element-to-element basis. This is again done with matrix logic by two 48×48 matrices (SM1-SM2). Only combinations agreeing with the kinematics of elastic scattering are accepted.

At this level also information from the CEDARs and the threshold Cerenkov counters enters.

It is required, by the majority logic, that less than a maximum number of particles have hit the different hodoscopes.

In addition, it is required that the energy deposited in the calorimeters, is above a certain limit.

At high-t data-taking the hard-wired processor constitutes a third level of the trigger. It makes even more refined tests on the kinematics of the event using the information from the MWPCs (see section 6).

If all the tests are fulfilled, an interrupt is sent to the NORD10 on-line computer and the event is read out via CAMAC and written to tape.

During this time (of the order of a few ms), the formation of a new strobe is inhibited by the event flip-flop.

Fig. 15 schematically shows the data acquisition system.

8. Off-Line Analysis

The analysis is done in three steps, as indicated in fig. 16.

The PROG1 program reads the raw data tapes, unpacks and decodes the data, and performs the pattern recognition. Furthermore it reconstructs the vertex position and approximates the track momenta using quite crude methods.

In order to be a fast program, PROG1 does not make use of detailed magnetic field maps or equivalently slow magnetic field routines. The field is instead described by a few constants of proportionality, used in the momentum reconstruction algorithm.

PROG2 is a least squares fitting program, based on a Runge-Kutta method. In order to have an efficient fitting procedure, a method is developed which includes analytical computation of the derivatives of the track coordinates with respect to the initial values [7]. PROG2 uses a box-wise representation of the magnetic field by Chebyshev polynomials [8].

Vertex constraints are always imposed on the track fitting, whereas the kinematical constraints of different event hypotheses can be applied optionally.

PROG3 is a program package for detailed event study and final event selection. It includes PROG2 with kinematical constraints.

Usually PROG1 and PROG2 (without kinematical constraints) are run together without producing an intermediate data summary tape, DST1. An event is only fitted by PROG2 if it fulfills certain criteria. The most important of these is that the event should have correct charge combination (i.e. -+ for negative beam and ++ for positive beam). At medium-t only the charge of the foreward particle is determined.
Typical execution times for high-t data through PROG1 and PROG2 is 0.05 - 0.1 s per trigger on an IBM 370/168 computer. This time consumption is dominated by PROG1 since by far most of the triggers have wrong charge combination.

Typical execution times for PROG2 is 0.15 - 0.20 s per vertex (high-t data) on an IBM 370/168.

Table 3 shows an example of the analysis performance for a typical high-t run. χ_g^2 is the chi-squared from a geometrical fit (i.e. without the application of the kinematical constraints), and χ_k^2 is the chi-squared from a fit with both geometrical- (i.e. vertex-) and kinematical constraints.

9. High-t Event Selection

Since the medium-t data are only partly analyzed, we restrict this discussion to high-t data.

The elastic events from the high-t runs were selected according to the following criteria [9]:

(1) Threshold and differential Cerenkov counters:

Reaction	Criterion
$\pi p \to \pi p$	$C1*\overline{C3}*\overline{C4}$
$Kp \to Kp$	$\overline{C1}*C2*CEDAR2*\overline{C3}*\overline{C4}$
$pp \to pp$	$CEDAR1*\overline{C1}*\overline{C2}*\overline{C3}*\overline{C4}$

(2) The reconstructed vertex should fall inside the target volume

(3) One trigger should give less than a maximum number of vertices. This number was 20 for -20 GeV/c data and 10 for -30 and +20 GeV/c data.

(4) A fit without the application of kinematical constraints should give $\chi_g^2 < 40$.

(5) If the event was 3-prong (i.e. with a reconstructed beam) a combined geometrical and kinematical fit should give $\chi_k^2 < 100$.

(6) A combined geometrical and kinematical fit with nominal beam should give $\chi_k^2 < 40$.

Finally it was required that the trigger should give only one elastic event. If two or more elastic events were found in one trigger, it was interpreted as due to two or more slightly different possible extensions of tracks into the magnet. In such cases only the event with the lowest chi-squared was kept.

Figs. 17 a and b show the χ_k^2-distributions for the event samples $\pi^- p \to \pi^- p$ and $K^- p \to K^- p$, respectively, at 20 GeV/c, that were accepted by the criteria (1) - (5). A strong elastic signal is seen.

10. Corrections Applied to the Cross Sections

A series of corrections are applied to the incoming flux. Some of them vary from run to run and from period to period. Table 4 lists the correction factors for 20 GeV/c negative beam (high-t). The following corrections are applied:

- Saturation in the beam hodoscope.
  At the higher intensities the beam hodoscope suffers from saturation effects. This is taken into account by correcting for the deviation from the linear dependence of the beam hodoscope counts on the ionization chamber.

- Majority random veto.
  The majority logic gives a certain fraction of random vetoes. This fraction is measured during data-taking.

- Prompt random veto.
  The beam- and magnet-veto counters give (a small) fraction of random vetoes.

- Chamber efficiencies.
  The multiwire proportional chambers have different efficiencies which are calculated off-line after the track reconstruction.

- Overlap and δ-rays in the beam hodoscope.
  Due to the geometrical overlap structure of the beam hodoscope planes (*fig.*7) and δ-ray production, the beam hodoscope gives a slightly too high intensity. This correction factor is calculated.

- Absorption in target.
  This effect gives a smaller effective flux than that measured in the beam hodoscope

- Interactions in the beam hodoscope
  Inelastic interactions in the beam hodoscope give a similar effect as δ-ray production.

- μ-content of the beam.
  The beam contains a certain fraction of muons, being counted by the beam hodoscope.

- $K/\bar{p}$ content of the beam.
  The beam contains a certain fraction of K and $\bar{p}$(p). The π-flux is determined from beam hodoscope counts and must be corrected for this. The K/p flux, however, is determined from CEDAR counts, and are accordingly not given similar corrections.

- Geometrical efficiency of hodoscopes.
  Due to small gaps between hodoscope elements, the H1,H2 (H3) and the prompt hodoscopes have geometrical efficiencies less than 1.

Finally the background within the χ^2-cuts is estimated. Fitting the background by a straight line through the origin (fig. 17) gives the following rough estimates for the background:

Channel	Beam momentum	Background
$\pi^- p \to \pi^- p$	20 GeV/*c*	1%
$K^- p \to K^- p$	20 -"-	4%
$\pi^+ p \to \pi^+ p$	20 -"-	5%
$K^+ p \to K^+ p$	20 -"-	25%
$pp \to pp$	20 -"-	7%
$\pi^- p \to \pi^- p$	30 -"-	6%

The cross sections presented in the last part of this report are not corrected for background.

II. THE RESULTS

1. Two-body hadronic interactions at high energy

Hadron-hadron interactions have been extensively studied in the peripheral regions, both experimentally and theoretically.

For 2-body hadronic collisions the Regge pole model predicts the cross sections to behave like

$$\frac{d\sigma}{dt} = H(t).s^{2\alpha(t)-2} \quad ,$$

a power law in s, where the power is related to the t or u channel resonance spectrum. Experimentally the s-dependence in the peripheral region is observed to be [11]

$$s^{-2\pm2}$$

This is accounted for by assuming meson or baryon Regge-exchange in the t or u channel, or by Pomeron exchange.

The Pomeron exchange is often identified with diffraction scattering. From the ISR measurements one knows the asymptotically surviving part of diffraction scattering.

The Regge limit is defined as:

$$s \to \infty$$
$$t \quad \text{finite}$$

In this region the Regge pole model gives the correct s-dependence of the cross-sections and the s-independent t-structure, t-scaling.

Even if there are unresolved questions in the peripheral regions it is reasonable to assume that these will be resolved within the Regge-exchange picture if particle exchange is allowed.

The cross-sections for two-body hadronic reactions where Regge-exchange or diffraction is absent falls very rapidly with energy [11]. The energy dependence of the third "non-peripheral component" is at fixed c.m. scattering angle observed to be [11]

$s^{-10\pm2}$.

The differential cross-sections in the region around 90° c.m. scattering angle is observed to behave approximately as

$$\frac{d\sigma}{dt} = s^{-n} f(\cos\theta_{cm}) \quad [11,12],$$

a scaling law in $\tau = -t/s \propto 1 - \cos\theta_{cm}$.

The fact that the hadrons lie on Regge trajactories is regarded as evidence for a composite structure of the hadrons. However, the detailed structure of the compositness is not probed in the Regge region.

It can be argued that if the hadrons are bound states of a finite number of constituents the Regge behaviour, $s^{\alpha(t)}$, changes into a power behaviour at large t, s^{-n} [13].

A natural question is consequently if the coherent Regge contribution will vanish at large 4-momentum transfers and if the scaling law in the region:

$$\begin{aligned} &s \to \infty \\ &-t \to \infty \\ &\tau = -t/s \quad \text{finite} \end{aligned} \qquad (1)$$

reflects the properties of basic interactions at short distance.

The s and t dependence of the basic interactions are not known. However, in a scale invariant theory an exclusive cross section in the fixed angle limit can be written as [14]

$$\frac{d\sigma}{dt} = s^{T+U-N}(-t)^{-T}(-u)^{-U} .$$

If the fundamental interaction is quark-quark scattering and if the quark-quark scattering is canonical scale invariant it may be shown from dimensional arguments that in the region $s \to \infty$, $-t \to \infty$ and τ finite 2-body interactions should behave as

$$\frac{d\sigma}{dt} = s^{-n} f(\cos\theta_{cm}) ,$$

$n = N - 2$ when N is the number of valence quarks in the interaction.

The scaling laws have not yet a firm theoretical derivation. The experimental data are at relatively low energies. At higher energies there will be scale breaking corrections predicted from QCD. These corrections are not known.

There are several models for the constituent structure and the basic interactions [14, 15, 16, 17, 18, 19, 20]. The experimental data have not yet been able to distinguish between them.

We will not discuss any of these models. However, some of the experimental results are compared to the constituent interchange model, CIM, [14]. In this model it is assumed that gluonic exchange between quarks of different hadrons is suppressed. Gluonic exchange is only internal to the hadronic wave functions.

The CIM gives cross sections consistent with the dimensional counting rule:

$\pi^{\pm}p$ and $K^{\pm}p$:

$$\frac{d\sigma}{dt} = s^{-8} f_M(\cos\theta_{cm})$$

$\bar{p}p$ and pp*):

$$\frac{d\sigma}{dt} = s^{-10} f_B(\cos\theta_{cm}) \qquad (1)$$

f_M and f_B are model dependent. In CIM they depend on the constituent structure of the scattered particles [14]. We list them for later references:

$$f_{\pi^+p} = \frac{\sigma_o}{s^8} \frac{(1+z)}{(1-z)}^4 (4\alpha(1+z)^{-2} + \beta)^2$$

$$f_{\pi^-p} = \frac{\sigma_o}{s^8} \frac{(1+z)}{(1-z)^4} (4\beta(1+z)^{-2} + \alpha)^2 \qquad (2)$$

$$f_{K^-p} = \frac{\sigma_o}{s^8} \frac{1+z}{(1-z)^4} \alpha^2$$

$$z = \cos\theta_{cm}$$

α and β are the relative weights of 2 amplitudes and is assumed to be $\alpha=2$ and $\beta=1$. CIM also assumes that σ_o, α and β are the same for π^+p, π^-p, K^+p and K^-p elastic scattering.

Before we present data from the present experiment we will briefly review some published data at lower energies.

*) The CIM predicts an asymptotic fixed angle cross section of the form

$$\frac{d\sigma}{dt} \sim s^{-n} f(\cos\theta_{cm})$$

n can be determined by the asymptotic fall-off of the form factors. In the model this fall-off depends on the composite model of the hadron. Depending on whether the nucleon is considered to be a bound state of three equivalent quarks or of a quark and a core, two-particle approximation, two alternative predictions are given for n in (antinucleon) nucleon-nucleon scattering. In the former case n=10, in the latter n=12. n=10 is consistent with the dimensional counting rule.

Figures 18, 19 and 20 show elastic differential cross sections, $\frac{d\sigma}{dt}$, for Kp, πp and $\bar{p}p$ respectively, as functions of t and $\cos\theta_{cm}$.

We summarize the following features.

1. Peripheral peaks dominate the cross sections.

2. Slow s-dependence of the pheripheral peaks. A fast decrease with s in the large angle region.

3. The structures in the cross sections disappear with s in the large angle region. In the peripheral regions the structures occurs at approximately fixed values of t, independent of s.

These gross features may be explained by Regge and diffraction contributions in the peripheral regions. Because of the exponential t-dependence of this amplitude its contribution disappears at large scattering angles as energy increases. In the large angle region the amplitude is eventually described by the dynamics governing the interaction between the constituents. If the constituents are structureless and their interaction is canonical scale invariant the energy dependence of the cross section in the high s and large -t region will be a power in s. The power will by dimensional arguments be given by the number of constituents.

2. Results on wide angle scattering

The new data we are presenting are preliminary. They will soon be published in their final version.

We will first discuss data in the wide angle scattering region.

Figures 21, 22 and 23 show our wide angle scattering data for π^-p, π^+p and K^-p elastic reactions respectively.

The new data are obtained, for the negative beam at the momenta 20 and 30 GeV/c and for the positive beam at 20 GeV/c. Data at lower energies are shown for comparison.

The number of accepted elastic events at 20 GeV/c are for π^-p scattering 38, for π^+p scattering 66 and for K^-p scattering 4. At 30 GeV/c the numbers are 26 events for π^-p scattering and 1 event for K^-p scattering.

The curves are calculated using CIM. The model was normalized to the π^+p results at 20 GeV/c, and then scaled according to the dimensional scaling law to the other energies according to (1) and (2).

Although the shape of the angular distributions are roughly correct the normalization disagrees with the data. This is particularly clear for the K^-p data.

Fig. 24 shows the π^-p elastic differential cross section, $\frac{d\sigma}{dt}$, at 90^o cm. scattering angle, from 2.5 GeV/c and up to 30 GeV/c beam momentum. The data are consistent with dimensional scaling for the momenta above 3.5 GeV/c. In this energy range the cross section decreases from 10^{-30} $cm^2/(GeV/c)^2$ to approximately 10^{-37} $cm^2/(GeV/c)^2$.

Fig. 25 shows the K^-p elastic differential cross section, $\frac{d\sigma}{dt}$, at 90^o and at 60^o cm scattering angles. The momenta range from 5 GeV/c and up to 30 GeV/c. The data point at 20 GeV/c and 90^o cm scattering angle is an upper limit. At 60^o cm scattering angle the results are consistent with the dimensional counting rule through the whole energy range considered. The cross sections range from about $5 \cdot 10^{-30}$ $cm^2/(GeV/c)^2$ to about 10^{-35} $cm^2/(GeV/c)^2$.

It has been suggested that p_T, the transverse momentum, could be a more relevant parameter than s to describe the wide angle data, as for example in the dual multiperipheral model [21].

In figures 26 and 27 we show the π^-p and π^+p elastic differential cross sections, $\frac{d\sigma}{dt}$, at 90^o cm scattering angle as function of p_T.

The data are well described by one exponential in p_T from 3.5 GeV/c. Within the observed energy range and with the presisions of the observations the data are equally well described by an exponential in p_T as a power in s.

The conclusions we draw from this presentation is that the dimensional counting rule holds from about 3.5 GeV/c and through the energy range considered. This energy range corresponds to seven orders of magnitude of the cross sections. However CIM in its simple form (2) is inconsistent with the data.

3. $\bar{p}p$ elastic scattering in the medium t region

We will next discuss some preliminary data from a study of $\bar{p}p$ elastic scattering in the interval $1(GeV/c)^2 \leq -t \leq 3.5\ (GeV/c)^2$ at 50 GeV/c.

The $\bar{p}p$ elastic differential cross section, $\frac{d\sigma}{dt}$, is shown in figure 28.

The total $\bar{p}p$ cross section at 50 GeV/c is 43.9 mb [22]. At 1480 GeV/c the total pp cross section is 43.0 mb [23]. The pp elastic differential cross section at this energy is drawn in figure 28. The cross sections overlap within the experimental resolution. (See footnote on the next page).

The dip at $-t \sim 1.4\ (GeV/c)^2$ in the pp elastic differential cross section is usually interpreted as a diffraction dip. At lower momenta the $\bar{p}p$ elastic differential cross section has a dip at $-t \sim 0.5\ (GeV/c)^2$ (fig. 20). This dip shows a tendency to move to higher values of $-t$ as energy increases [24]. If this dip is a diffraction dip one would expect that it moves according to the geometrical scaling law as observed in pp elastic scattering:

$$-t_{dip} \sim \frac{1}{\sigma_{tot}}$$

The total $\bar{p}p$ cross sections are 65 mb and 44 mb at 5 GeV/c and 50 GeV/c respectively. If geometrical scaling is valid one would expect the dip to occur at $-t \sim 0.8\ (GeV/c)$ at 50 GeV/c.

In figure 20 (and 29) we observe, however, that a shoulder is developing around $-t \sim 2\ (GeV/c)^2$. This shoulder could conceivably be identified with the dip at $-t \sim 1.4\ (GeV/c)^2$ seen at 50 GeV/c.

Assuming the amplitude to be entirely imaginary the following relation follows from the geometrical scaling law [25]

$$\frac{d\sigma}{dt}(s_1,t_1) = \frac{\sigma^2_{tot}(s_1)}{\sigma^2_{tot}(s_2)} \cdot \frac{d\sigma}{dt}(s_2,t_2 = \frac{\sigma_{tot}(s_1)}{\sigma_{tot}(s_2)} \cdot t_1)$$

In figure 29 we compare the cross section at 50 GeV/c (s_2) with the cross section at 10.0 GeV/c (s_1). Geometrical scaling is badly broken in $\bar{p}p$ scattering in this energy range.*)

In figure 30 we show the elastic differential cross section, $\frac{d\sigma}{dt}$, as a function of s, at a scattering angle of 21.6° in the cm system. The decrease with s is much slower than expected from the dimensional counting rule.

The peripheral part of the pp elastic differential cross section, $\frac{d\sigma}{dt}$, seems to approach an asymptotic limit at the highest ISR energies. This is shown in the figures 31, 32 and 33 for $t = -1.4$ $(GeV/c)^2$, $t = -2.5$ $(GeV/c)^2$ and $t = -3.0$ $(GeV/c)^2$ respectively [43,44].

In these figures we have also plotted the $\bar{p}p$ elastic differential cross sections at the same values of t.

The $\bar{p}p$ cross section at fixed t decreases as a power of s, typical for the Regge exchange region. There is no tendency for a levelling off of the cross section. In a region where diffraction scattering dominates one expects a much slower s-dependence, as is observed in pp elastic scattering.

*) We believe that the cross section at 50 GeV/c is around a factor 3 too low. (Latest from the analysis.)

Assuming the amplitude to be entirely imaginary the following relatio follows from the geometrical scaling law [25]

$$\frac{d\sigma}{dt}(s_1,t_1) = \frac{\sigma^2_{tot}(s_1)}{\sigma^2_{tot}(s_2)} \cdot \frac{d\sigma}{dt}(s_2,t_2 = \frac{\sigma_{tot}(s_1)}{\sigma_{tot}(s_2)} \cdot \quad _1)$$

In figur 29 we compare the cross section at 50 eV/c (s_2) with the cross secti at 10.0 GeV/c (s_1). Geometrical aling is badly broken *in* $\bar{p}p$ *scatt ing in this energy range.**)

In figure 30 we ow the elastic differe ial cross section, $\frac{d\sigma}{dt}$, as a function of s, at a scattering angle o 21.6° in the cm system. The decrease with s is uch slower th expected from the dimensional counting rule.

The peripheral part of the elastic differential cross section, $\frac{d\sigma}{dt}$, seems to approach an asymp limit at the highest ISR energies. This is shown in the figures 31 32 a 33 for t = -1.4 $(GeV/c)^2$, t = -2.5 $(GeV/c)^2$ and t = -3.0 $(GeV/c)^2$ r pectively [43,44].

In these figures w ave also plotted th $\bar{p}p$ elastic differential cross sections at the sa e values of t.

The $\bar{p}p$ cr s section at fixed t decreases a power of s, typical for the Re ge exchange region. There is no te dency for a levelling off of e cross section. In a region where di fraction scattering domina s one expects a much slower s-dependence, as is observed in elastic scattering.

*)We believe that the cross section at 50 GeV/c is around a factor 3 too low. (Latest from the analysis.)

TABLE 1 Properties of C1, C2, C3 and C4
The fillings refer to 20 GeV/c beam momentum.

		Volume (m^3)	Length along z (m)	Gas	Refr.ind. $(n-1)\cdot10^6$	Rad.length (m)	Thresholds (GeV/c) π	K	p
Fast arm	C1	39	4.6	N_2	269	304	6.0	21.1	40.5
	C2	45	3.6	Freon 12*	1013	48	3.1	10.9	20.9
Slow arm	C3	17	1.6	Freon 12*	1013	48	3.1	10.9	20.9
	C4	31	2.5	CO_2	405	202	4.9	17.2	33.0

* Chemical formula is CCl_2F_2

TABLE 2. Properties of the Multi Wire Proportional Chambers

Chamber	Plane	Projection	Wire spacing	No. of wires
CHO	1	v	2	224
	2	y	2	96
	3	u	2	224
	4	x	1	384
CH1	1	x	1	960
	2	u	2	384
	3	y	2	128
	4	v	2	384
	5	x	1	960
CH2	1	x	1	1088
	2	v	2	448
	3	u	2	448
CH3	1	x	2	1024
	2	u	2	768
	3	v	2	768
	4	y	2	288
	5	x	2	1024
	6	x	2	1024
CH4	1	u	2	800
	2	y	2	1184
	3	v	2	800
	4	x	2	1184
CH5	1	x	2	608
	2	u	2	800
	3	y	2	608
	4	v	2	800
CH6	1	x	2	1184
	2	u		800
	3	y		1184
	4	v		800
CH7	1	y		288
	2	x		672
	3	β	2	96
CH8	1	y	2	288
	2	x	2	672
	3	β	2	96
CH9	1	y	2	288
	2	x	2	672
	3	β	2	96
CH10	1	y	2	288
	2	x	2	672
	3	β	2	96

The β-projection is only slightly different from the u projection.

TABLE 3. Trigger and Analysis Performance of a typical high-t run.

TRIGGER	No. of bursts	428
	No. of integrated burstscalers	1.3×10^{10}
	No. of fast strobes (ungated)	5.5×10^{6}
	No. of triggers to tape	4.7×10^{4}
PROG1	No. of triggers input	$4.7\ 10^{4}$
	No of triggers accepted	9299 (20%)
PROG2 WITHOUT KINEMATICS	No. of triggers input	9299
	No. of events input	11336
	No. of events with correct charge comb.	466
	No. of events accepted, $\chi^2_g < 100$	263
PROG2 WITH KINEMATICS	No. of events input	263
	No of events with $\chi^2_k < 500$	30
	No of events with $\chi^2_k < 40$	2

TABLE 4. Summary of Correction Factors, 20 GeV/c negative beam.

Correction	Particle-Indep. factors	Particle-Dep. factors		
		π	K	p
Saturation in beam hodoscope	1.01			
Majority random veto	0.53			
Prompt random veto	0.99			
Chamber efficiencies	0.76			
Live-time	0.63			
Overlap and δ-rays		0.88		
Interactions in beam hodoscope		0.97	0.98	0.96
Absorption in target		0.95	0.95	0.95
μ-content of the beam		0.94		
$K/\bar{p}$ content of the beam		0.95		
Geometrical efficiency of hodoscopes		0.97	0.97	0.97

FIGURE CAPTIONS

Fig. 1 Location of WA7 in the SPS West Experimental Area (from [10]).

Fig. 2 Experimental lay-out, high-t arrangement.

C1 - C4	threshold Cerenkov counters
CH1 - CH6	multiwire proportional chambers
H1 - H2	scintillation counter hodoscopes
PH1 - PH2	scintillation prompt hodoscopes
M	spectrometer magnet

Fig. 3 Experimental lay-out, medium-t recoil arm.

CH0 - CH1, CH7 - CH10 multiwire proportional chambers

CP1	threshold Cerenkov counter
AC	aerogel threshold Cerenkov counter
V	veto counter

Fig. 4 The E1B/H1B beam line (from [10], but slightly updated).

BEND, TR	dipole bending magnets
Q	quadrupole magnets
CH	horizontal collimators
CV	vertical collimators

$1.2\ S_x(2.8\ S_y)$ corresponds to the deviation in x (y) from the central beam line of a particle which was produced at central beam line with an angle in x (y) of 1.2(2.8) mrad. These are the maximum angles accepted.

Fig. 5 E1/H1 beam calculated intensities per 10^{12} interacting protons (from [10]).

Fig. 6 CEDAR2 scanned.

Fig. 7 Arrangement of scintillators in a beam hodoscope plane.

Fig. 8 Multiwire proportional chamber coordinates.
The beam moves in positive z-direction. Note that chamber CH5 has its own coordinate system since the whole chamber is rotated 45^{o} for acceptance reasons.

$\sin\theta = 8/17$ is chosen to facilitate the reconstruction in an on-line hard-wired processor with 16 bit word length.

Fig. 9 Structure of the H1, H2 and H3 hodoscopes.

Fig. 10 Structure of the PH1, PH2 and PH3 prompt hodoscopes.

Fig. 11 Principle of a prompt hodoscope element (from [5]).

Fig. 12 Arrangement of a prompt hodoscope element (from [5]).

Fig. 13 a) The iron calorimeters.

Fe	$200\times200\times10$ cm^3 iron plates
Scintil	scintillator counter planes
MWPC	multiwire proportional chamber planes

b) A scintillation counter plane in the calorimeter.

Fig. 14 The trigger logic without processor.
See the text.

Fig. 15 The data acquisition system.

Fig. 16 The analysis chain.
See the text.

Fig. 17 a) Chi-squared distribution from fit with nominal beam and kinematical constraints for $\pi^-p \to \pi^-p$ events at 20 GeV/c which were accepted by the requirements (1)-(5).
See the text.

b) As a), but for $K^-p \to K^-p$ events.

Fig. 18 $K^{\pm}p$ elastic differential cross sections. [26, 27, 28].
- a) K^-p cross sections as a function of cosine to the c.m. scattering angle, $\cos\theta_{cm}$.
- b) As a) but as a function of the squared four momentum transfer, $-t$.
- c) K^+p cross sections as a function of cosine to the c.m. scattering angle.
- d) As c) but as a function of the squared four momentum transfer.

Fig. 19 $\pi^{\pm}p$ elastic differential cross sections. [26, 29, 27].
- a) π^-p cross sections as a function of cosine to the c.m. scattering angle.
- b) As a) but as a function of the squared four momentum transfer.
- c) π^+p cross sections as a function of cosine to the c.m. scattering angle.
- d) As c) but as a function of the four momentum transfer squared.

Fig. 20 $\bar{p}p$ elastic differential cross sections [30].
- a) As function of cosine to the c.m. scattering angle.
- b) As function of the squared four momentum transfer.

Fig. 21 π^-p elastic differential cross sections as function of cosine to the c.m. scattering angle. [26, 31, 32].

Fig. 22 π^+p elastic differential cross sections as function of cosine to the c.m. scattering angle [33].

Fig. 23 K^-p elastic differential cross section as function of cosine to the c.m. scattering angle, from this experiment and from ref. [26].

Fig. 24 The elastic differential π^-p scattering cross section at 90^o in the c.m. system as function of the squared c.m. energy. [34, 35, 31].

Fig. 25 The elastic differential K^-p scattering cross section at 90^o and 60^o in the c.m. system as function of the squared c.m. energy. [35, 26, 36].

Fig. 26 The elastic differential π^-p scattering cross section at 90^o in the c.m. system as a function of the transverse momentum. Ref. see fig. 24.

Fig. 27 As fig. 26 for π^+p. [34, 26, 27].

Fig. 28 The elastic differential $\bar{p}p$ scattering cross section as function of the squared four momentum transfer. [25]. (See footnote p. 24).

Fig. 29 Comparison of the differential cross sections at $\sqrt{s}_1 = 4.5$ GeV [37]. The cross sections and t values at $\sqrt{s}_2 = 95.65$ GeV have been scaled according to geometrical scaling, see p. 24. (See footnote p. 24).

Fig. 30 The elastic differential $\bar{p}p$ cross section at 21.6^o in the c.m. system as function of the squared c.m. energy. [38, 39, 40,41, 42].

Fig. 31 The elastic differential $\bar{p}p$ and pp cross sections as function of the squared c.m. energy at $-t = 1.4$ $(GeV/c)^2$. [35, 31, 30, 42, 43].

Fig. 32 As fig. 31 at $-t = 2.5$ $(GeV/c)^2$. [31, 37, 43].

Fig. 33 As fig. 31 at $-t = 3.0$ $(GeV/c)^2$. [31, 37, 43].

REFERENCES

[1] T. Buran et. al., CERN/SPSC 74-28 (1974)

[2] C. Bouvet et. al., CERN/Lab. II/EA/74-4 (1975)

[3] P. Carlson and R. Kiesler, CERN-EP/79-09 (1979)

[4] P. Carlson and M. Poulet, Nucl. Instr. & Meth. 166 (1979) 425

[5] M. Poulet and A. Santroni, Nucl. Instr. & Meth. 148 (1978) 359

[6] I. Gjerpe, WA7 Internal Report, ELAS 137 (1979)

[7] J. Myrheim and L. Bugge, Nucl. Instr. & Meth. 160 (1979) 43

[8] R. Bøck and J. Myrheim, WA7 Internal Report, ELAS 95 (1976)

[9] K. Brobakken, P. Helgaker and J. Myrheim, WA7 Internal Reports, ELAS 134, 135, 136 (1980)

[10] SPS Experimenters' Handbook, CERN (1978)

[11] A. Lundby, Fifth International Conference on High-Energy Collisions, Stony Brook, NY, USA, 23.-24. August 1973

[12] J.F. Gunion, S.J. Brodsky and R. Blankenbecler, Physical Rev., 8, 287 (1973)

[13] D. Amati, L. Caneschi and M. Testa, Th 1644 - CERN (1973)

[14] R. Blankenbecler, S.J. Brodsky and J.F. Gunion, Phys. Lett. 39B, 649 (1972), SLAC-PUB-2057 (1977)

[15] D. Horn and M. Moshe, Nucl. Phys. B48 (1972)

[16] P.V. Landshoff, DAMTP 73/36, DAMTP 77/28

[17] V.A. Matveev, R.M. Muradyan and A.N. Tavkelidze, Lett. Nuovo Cim. 5, 907 (1972)

[18] S.J. Brodsky and G.R. Farrar, Phys. Rev. Lett. 31, 1153 (1973)

[19] D. Cline, F. Halzen and M. Waldrop, Nucl. Phys. B55, 157 (1973)

[20] P. Fishbane and C. Quigg, Nucl. Phys. B61, 469 (1973)

[21] B. Schrempp and F. Schrempp, Phys. Lett. 55B, 303 (1975)

[22] A.S. Carroll et al., Phys. Lett. 61B, 303 (1976)

[23] U. Amaldi et al., Phys. Lett. 44B, 112 (1973)

[24] P. Helgaker, Thesis, University of Oslo (1975)

[25] E. Nagy et al. CERN-PRE 78-137 (1978)

[26] T. Buran et al. Nucl. Phys. B111, 1 (1976)

[27] C. Baglin et al. Nucl. Phys. B98, 365 (1975)

[28] V. Chabaud et al. Phys. Lett. 38B, 445 (1972)

[29] C. Baglin et al. Phys. Lett. 47B, 85 (1973)

[30] T. Buran et al. Nucl. Phys. B97, 11 (1975)

[31] D.P. Owen et al., Phys. Rev. 181, 1794 (1969)

[32] P. Cornillon et al., Phys. Rev. Lett. 30, 403 (1973)

[33] C. Baglin et al., Phys. Rev. Lett. 40, 425 (1978)

[34] C.T. Coffin et al. Phys. Rev. 159, 1169 (1967)

[35] Å. Eide et al. Nucl. Phys. B60, 173 (1973)

[36] A. de Bellefon et al. CERN-PRE 78-147

[37] A. Berglund et al., CERN-PRE Nov. 1978

[38] O. Czyzewski et al., Phys. Lett. 15, 188 (1965)

[39] K. Boeckmann et al., Il Nuovo Cimento, 42B, 954 (1966)

[40] T. Kitagaki et al. Phys. Rev. Lett. 21, 175 (1968)

[41] K.J. Foley et al., Phys. Rev. Lett. 11, 503 (1963)

[42] D. Birnbaum, Phys. Rev. Lett. 23, 663 (1969)

[43] V. Barger, F. Halzen and R.J.N. Philips, University of Wisconsin Preprint 1973

[44] S. Conetti et al. CLNS - 409 (1978)

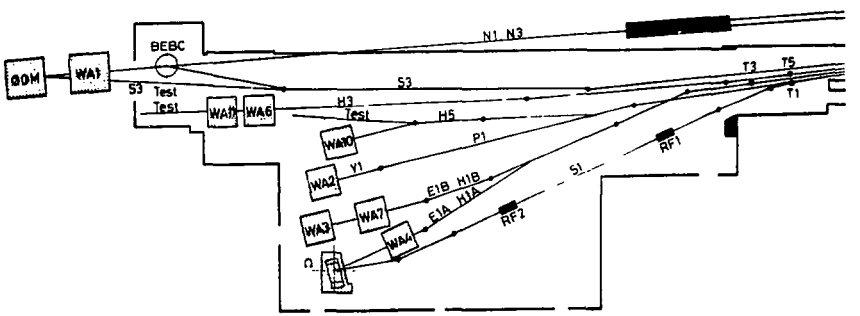
BEBC
N1 N3
S3
Test
Test
S3
H3
Test
H5
P1
Y1
E1B H1B
E1A H1A
S1
RF1
RF2
T3
T5
T1
WA1
WA2
WA3
WA4
WA5
WA6
WA7
WA10

Figure 1.

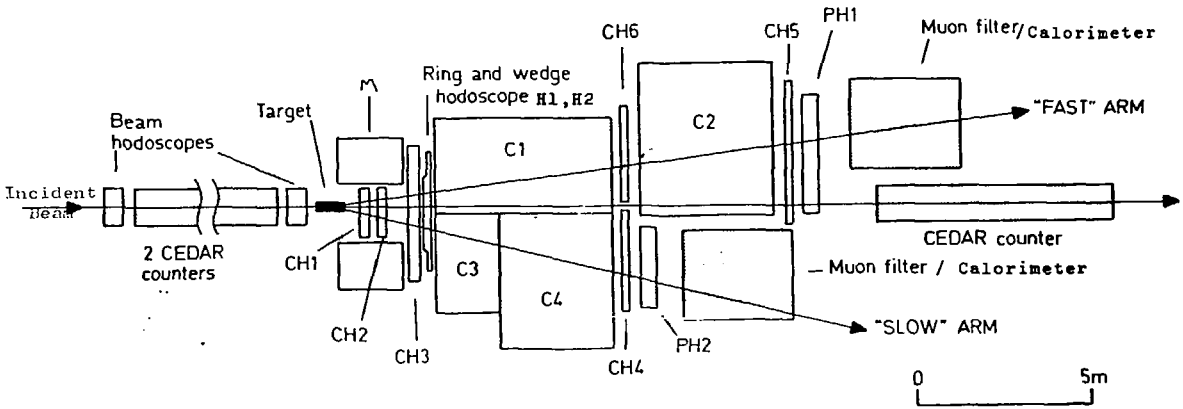
Incident Beam
Beam hodoscopes
2 CEDAR counters
Target
M
CH1
CH2
CH3
Ring and wedge hodoscope H1, H2
C1
C3
C4
CH4
CH5
CH6
C2
PH1
PH2
Muon filter/Calorimeter
"FAST" ARM
CEDAR counter
Muon filter / Calorimeter
"SLOW" ARM
0
5m

Figure 2.

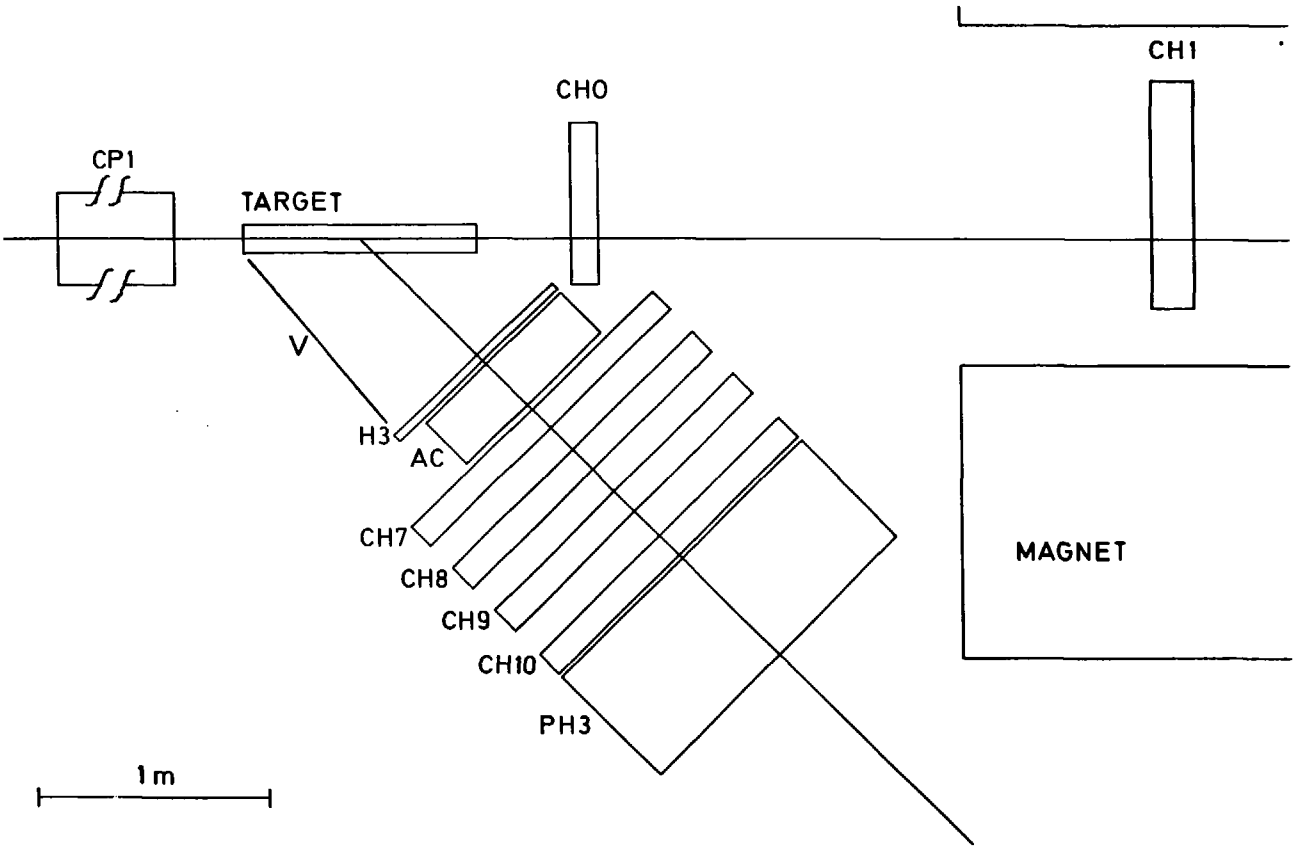

Figure 3.

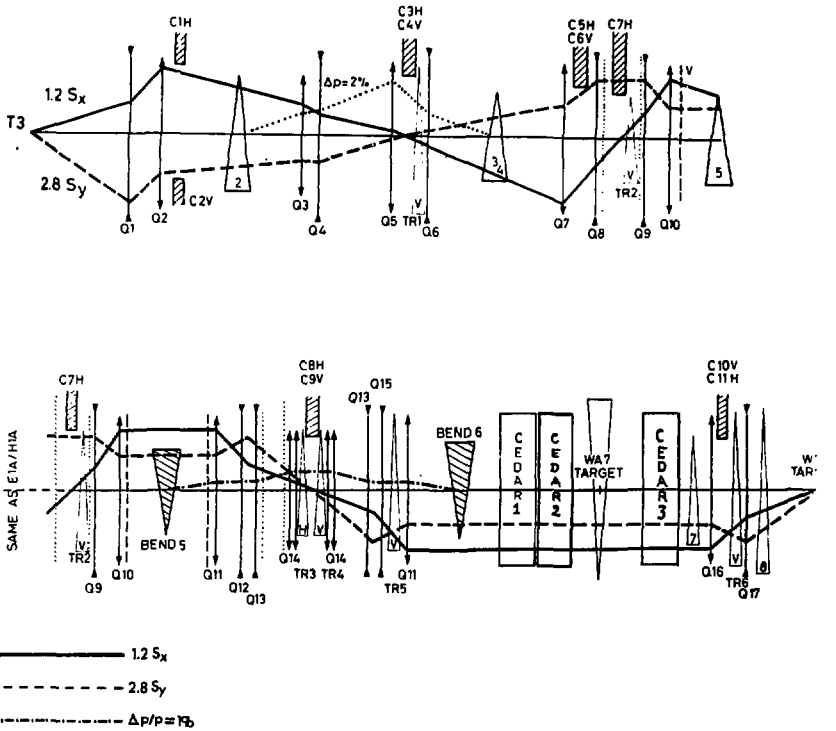
C1H
C3H
C4V
C5H
C6V
C7H
1.2 S_x
T3
2.8 S_y
Δp=2%
C2V
V
Q1
Q2
Q3
Q4
Q5
TR1
Q6
Q7
Q8
TR2
Q9
Q10
C7H
C8H
C9V
Q13
Q15
BEND 6
C10V
C11 H
SAME AS E1A/H1A
BEND 5
Q11
Q12
Q13
Q14
TR3
TR4
TR5
Q16
TR6
Q17
CEDAR 1
CEDAR 2
CEDAR 3
WA7 TARGET
1.2 S_x
2.8 S_y
$\Delta p/p = \pm 1\%$

Figure 4.

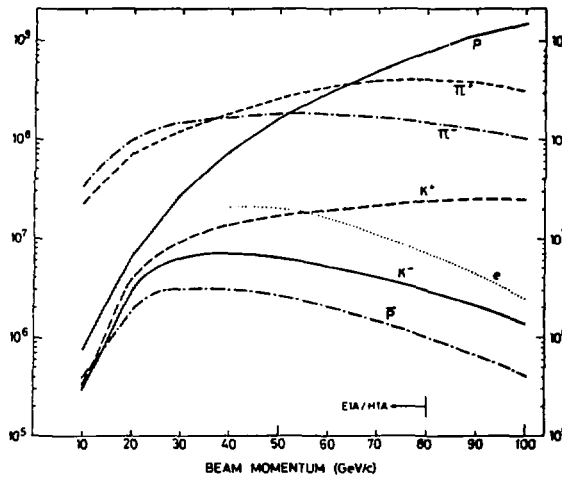
10^9
10^8
10^7
10^6
10^5
p
π^+
π^-
K^+
K^-
e
$\bar{p}$
E1A / H1A
10
20
30
40
50
60
70
80
90
100
BEAM MOMENTUM (GeV/c)

Figure 5.

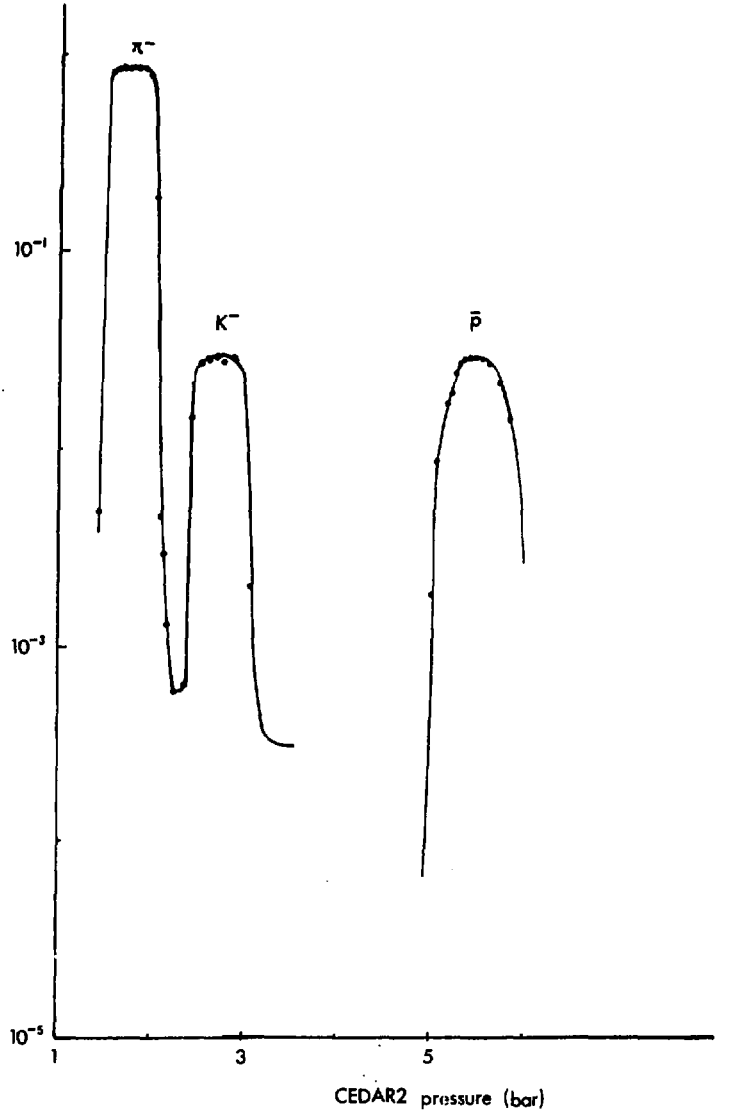

Figure 6.

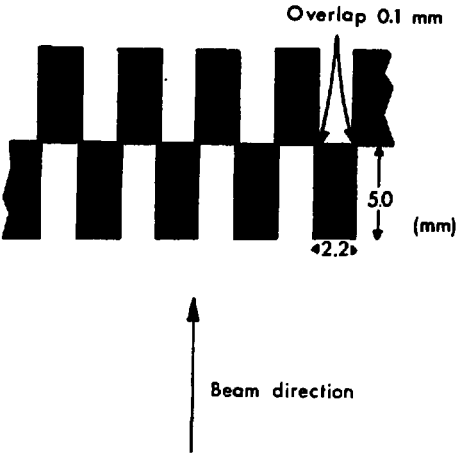

Figure 7.

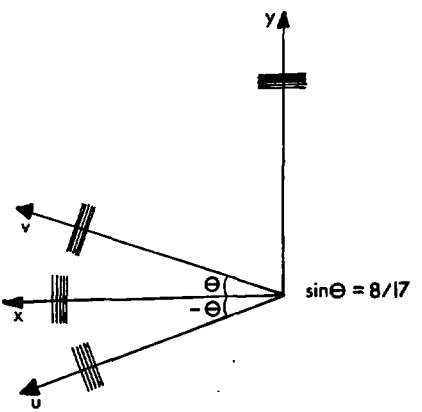

Figure 8.

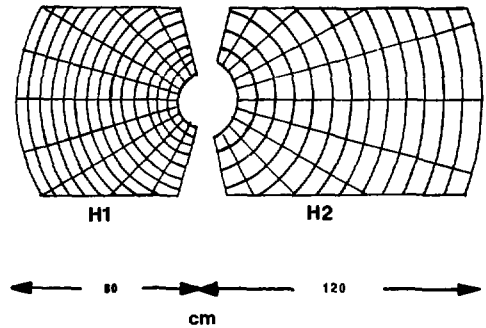

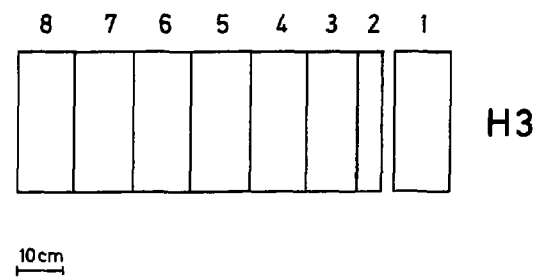

Figure 9.

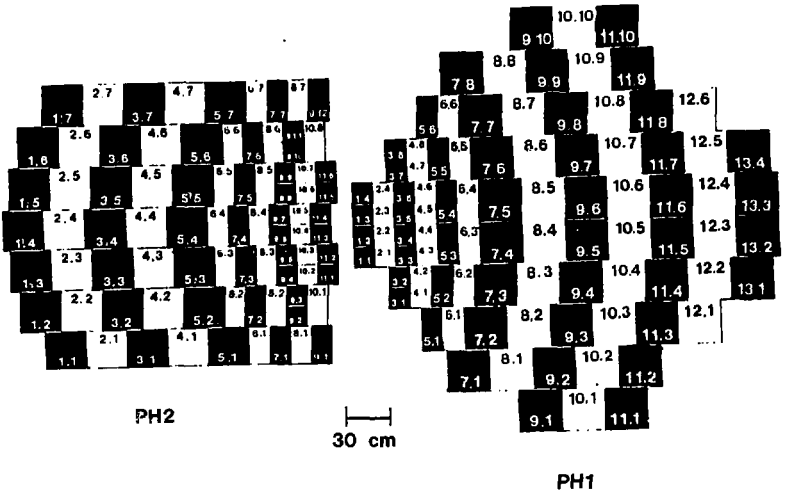

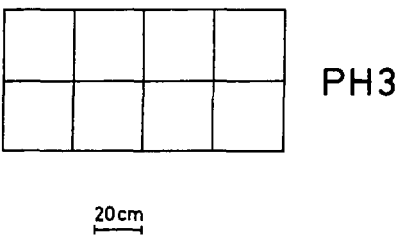

Figure 10.

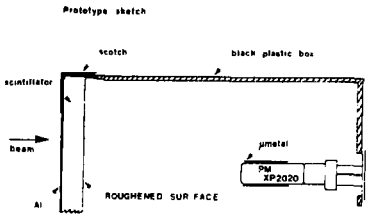

Figure 11.

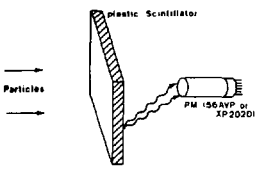

Figure 12.

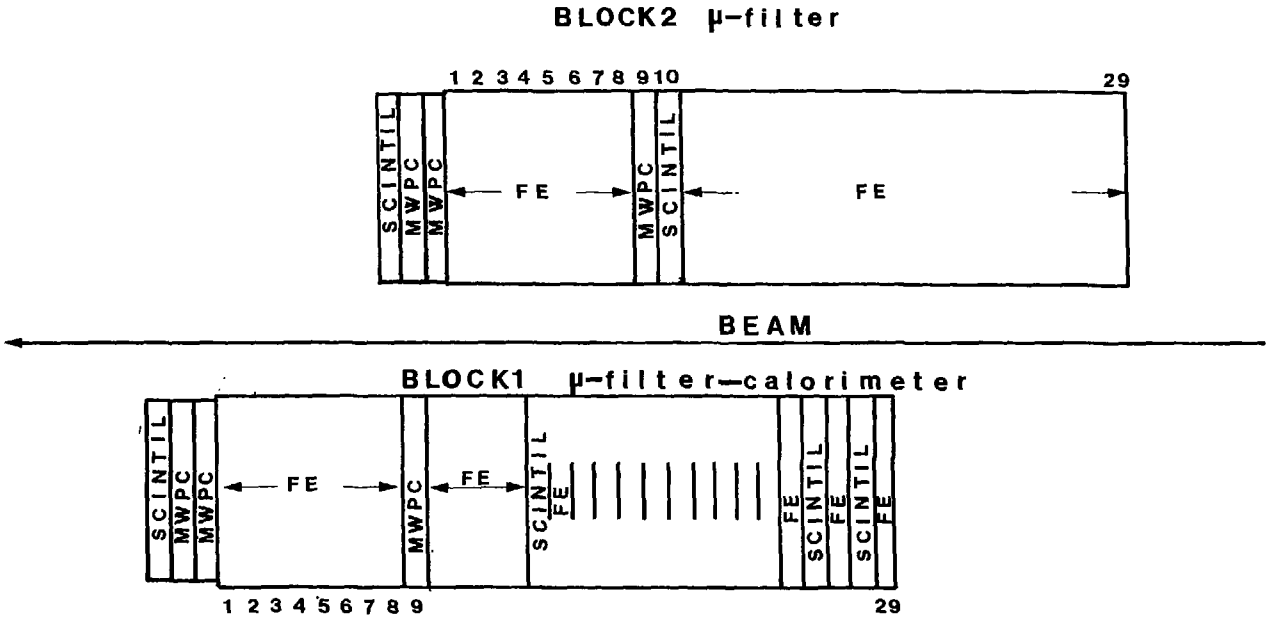
BLOCK2 μ-filter
1 2 3 4 5 6 7 8 9 10
29
SCINTIL
MWPC
MWPC
FE
MWPC
SCINTIL
FE
BEAM
BLOCK1 μ-filter-calorimeter
SCINTIL
MWPC
MWPC
FE
MWPC
FE
SCINTIL
FE
FE
SCINTIL
FE
SCINTIL
FE
1 2 3 4 5 6 7 8 9
29
μ-filter-calorimeter

Figure 13 (a).

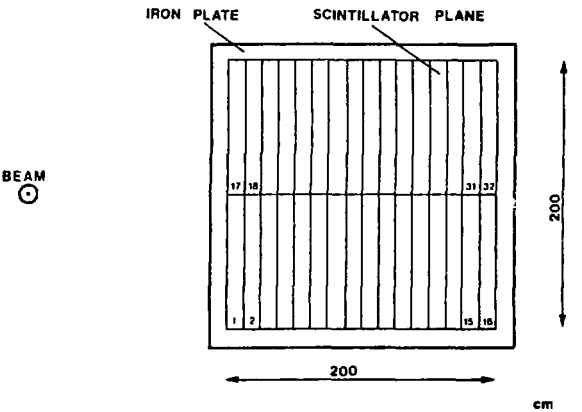
IRON PLATE
SCINTILLATOR PLANE
BEAM
17
18
31
32
1
2
15
16
200
200
cm

Figure 13 (b).

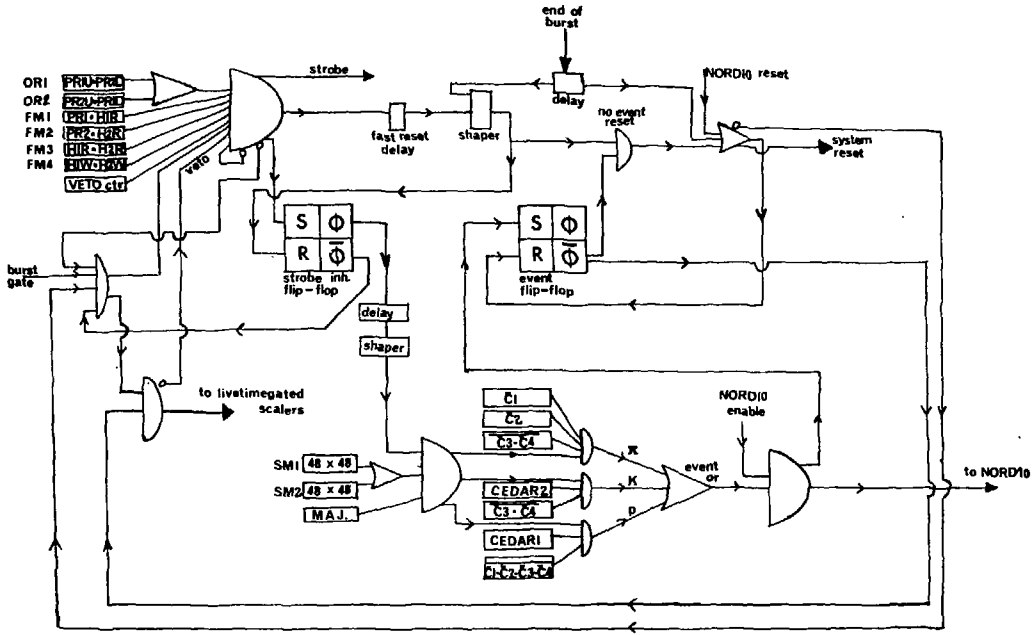
end of burst
strobe
delay
NORD10 reset
ORI
OR2
FM1
FM2
FM3
FM4
PRU·PRL
PR2U·PR2L
PRL·HIR
PR2·H2R
HIR·H1R
H1W·H2W
VETO ctr
veto
fast reset delay
shaper
no event reset
system reset
S
Φ
R
strobe inh. flip-flop
event flip-flop
burst gate
delay
shaper
to livetimegated scalers
C̄1
C̄2
C3·C4
NORD10 enable
SM1 48 x 48
SM2 48 x 48
MAJ.
CEDAR2
C3·C4
CEDAR1
C1·C2·C3·C4
π
K
p
event or
to NORD10

Figure 14.

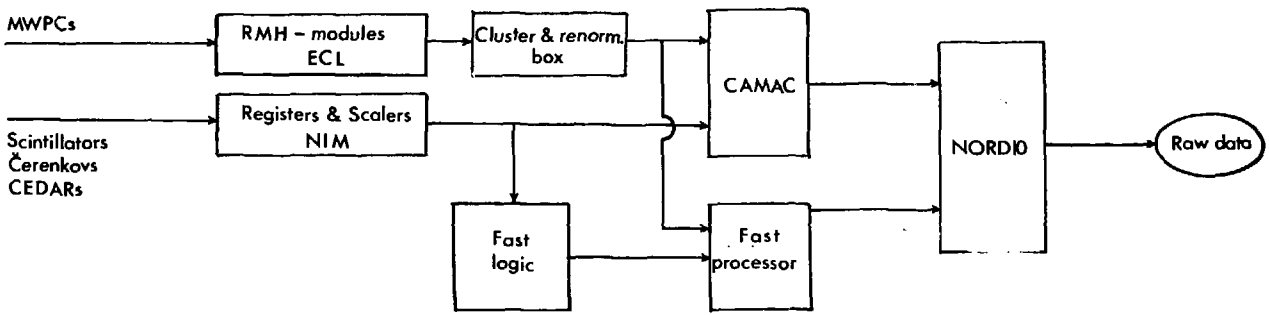
MWPCs
RMH – modules
ECL
Cluster & renorm.
box
CAMAC
Registers & Scalers
NIM
Scintillators
Čerenkovs
CEDARs
NORD10
Raw data
Fast
logic
Fast
processor

Figure 15.

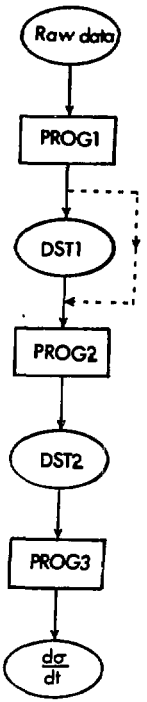

Figure 16.

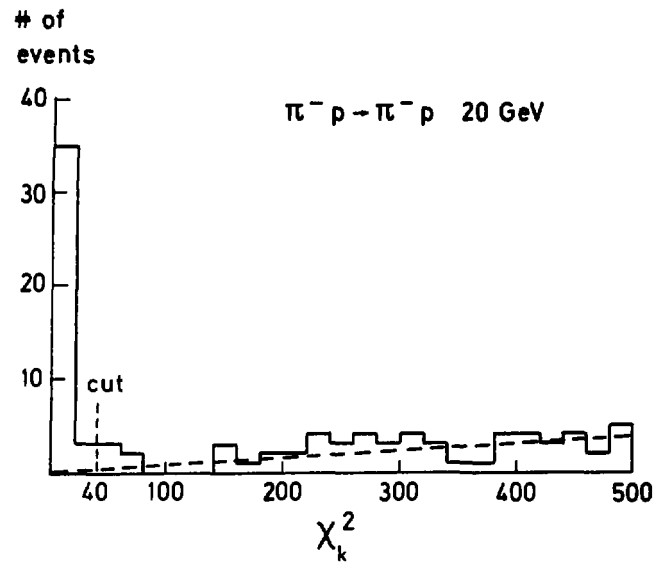
of
events
40
30
20
10
cut
$\pi^- p \to \pi^- p$ 20 GeV
40
100
200
300
400
500
χ^2_k

(a)

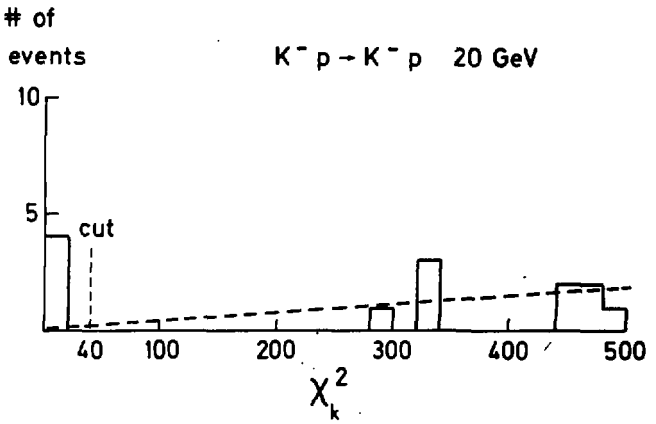
of
events
$K^- p \to K^- p$ 20 GeV
10
5
cut
40
100
200
300
400
500
χ^2_k

(b)

Figure 17.

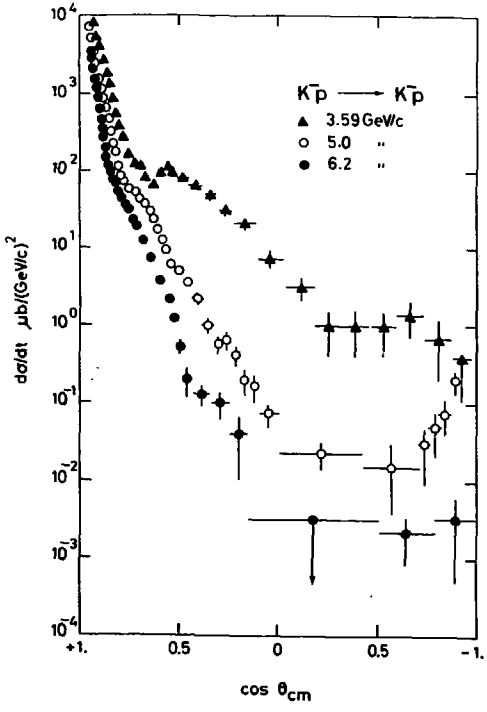

Fig. 18 a)

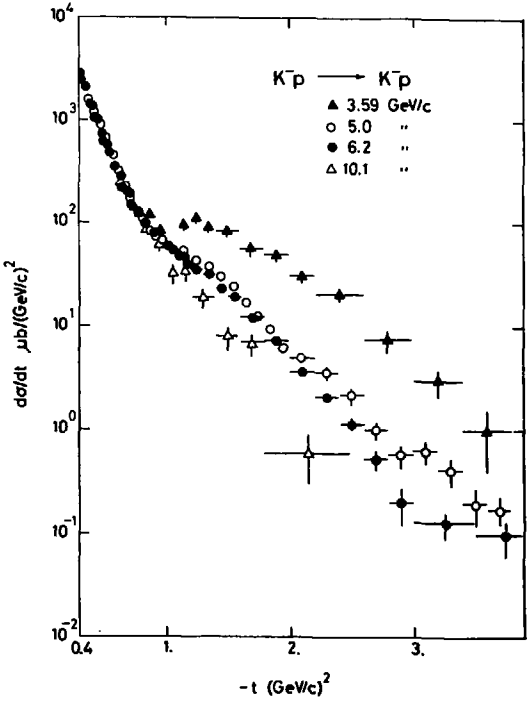

Fig. 18 b)

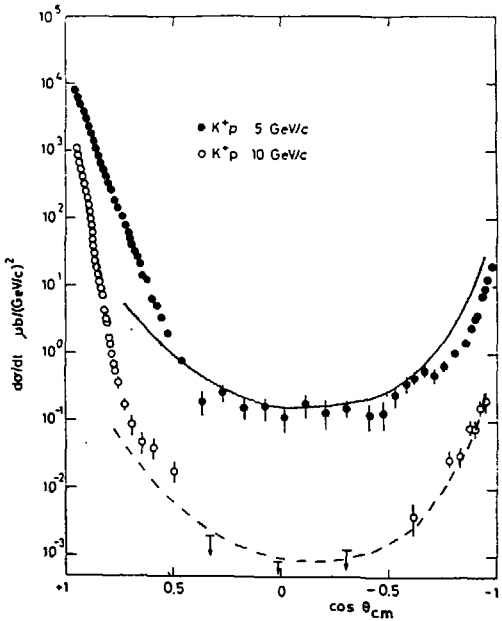

Fig. 18 c)

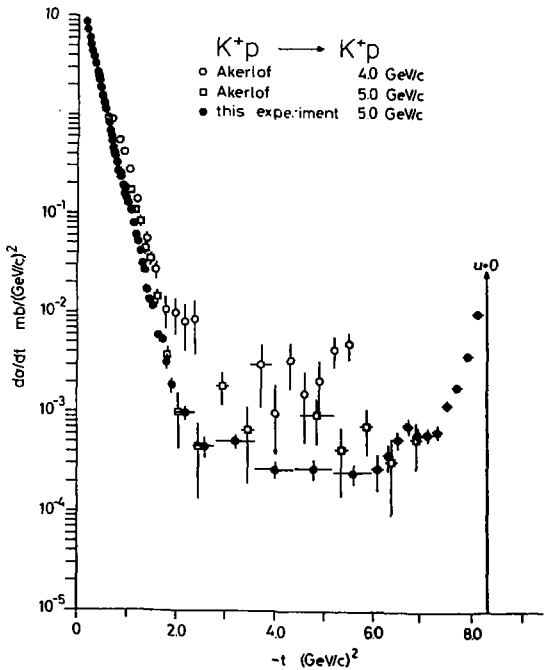

Fig. 18 d)

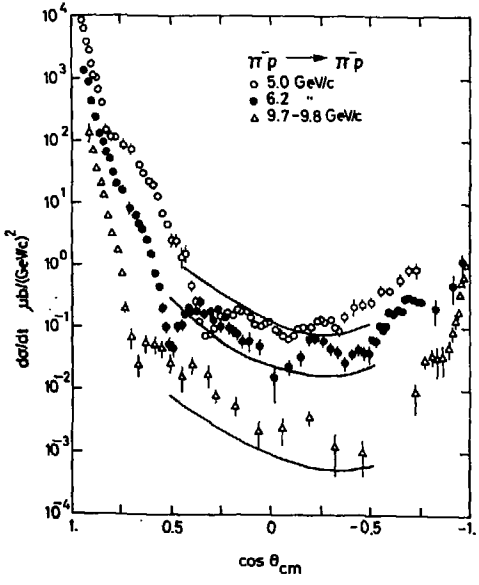

Fig. 19 a)

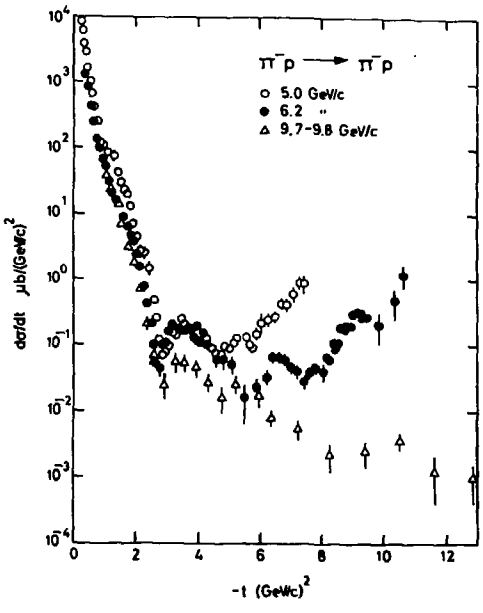

Fig. 19 b)

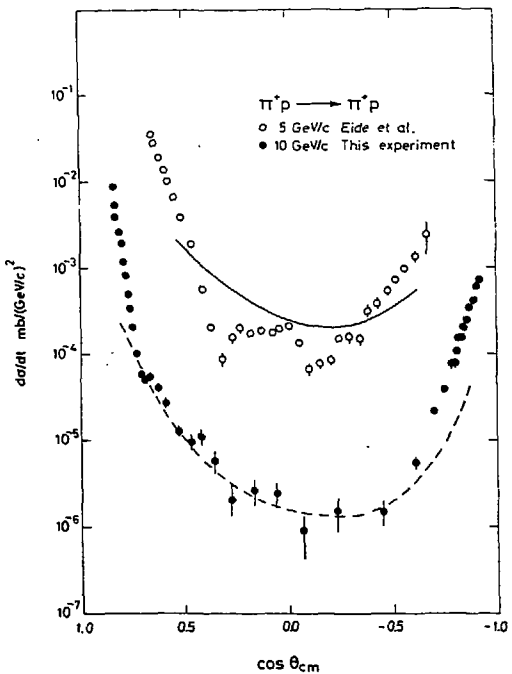

Fig. 19 c)

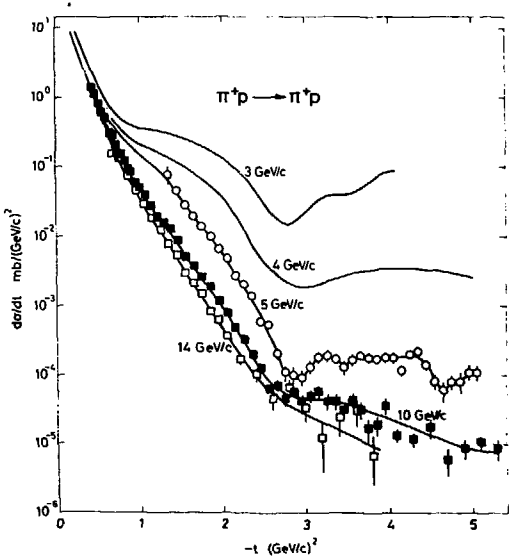

Fig. 19 d)

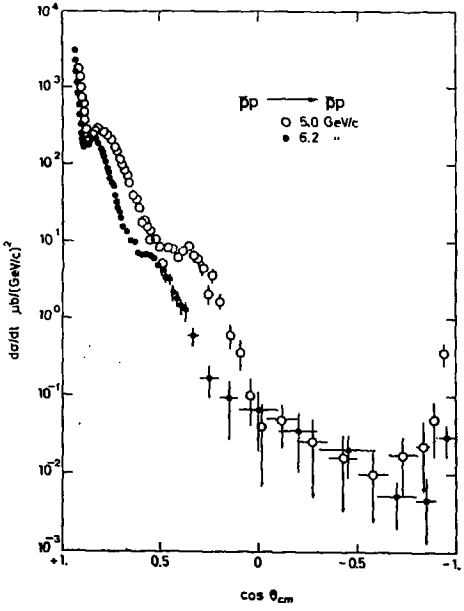

Fig. 20 a)

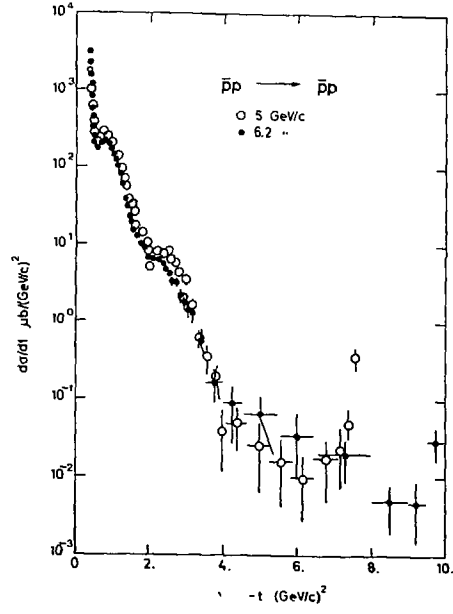

Fig. 20 b)

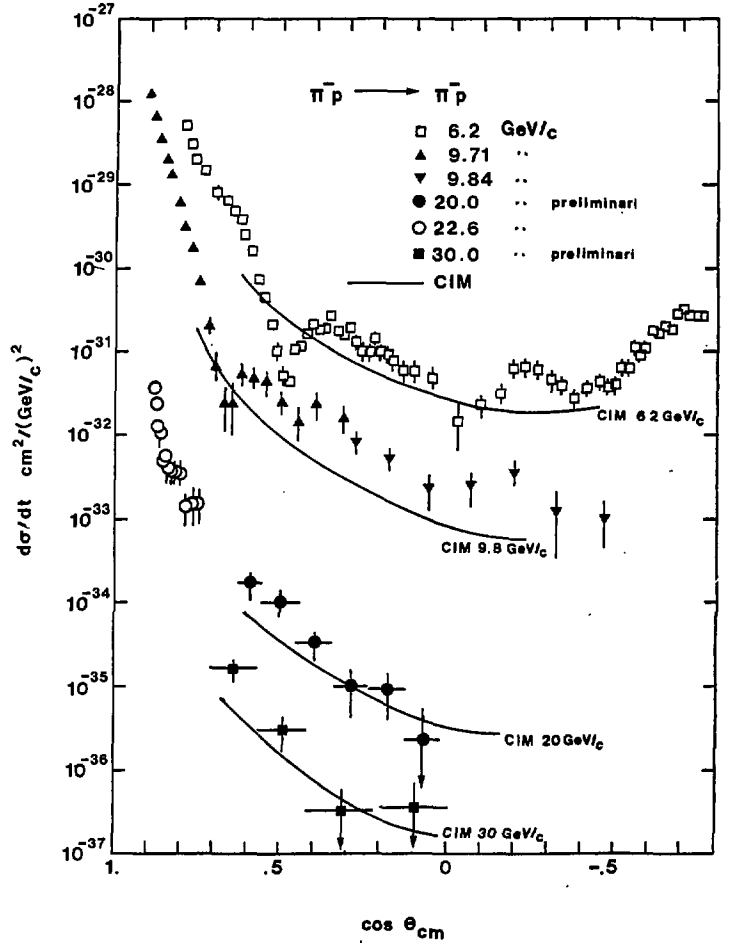
$\pi^- p \longrightarrow \pi^- p$
6.2 GeV/c
9.71 ··
9.84 ··
20.0 ·· preliminari
22.6 ··
30.0 ·· preliminari
CIM
CIM 6.2 GeV/c
CIM 9.8 GeV/c
CIM 20 GeV/c
CIM 30 GeV/c
$d\sigma/dt$ cm^2/(GeV/c)^2
10^{-27}
10^{-28}
10^{-29}
10^{-30}
10^{-31}
10^{-32}
10^{-33}
10^{-34}
10^{-35}
10^{-36}
10^{-37}
1.
.5
0
-.5
cos θ_{cm}

Fig. 21

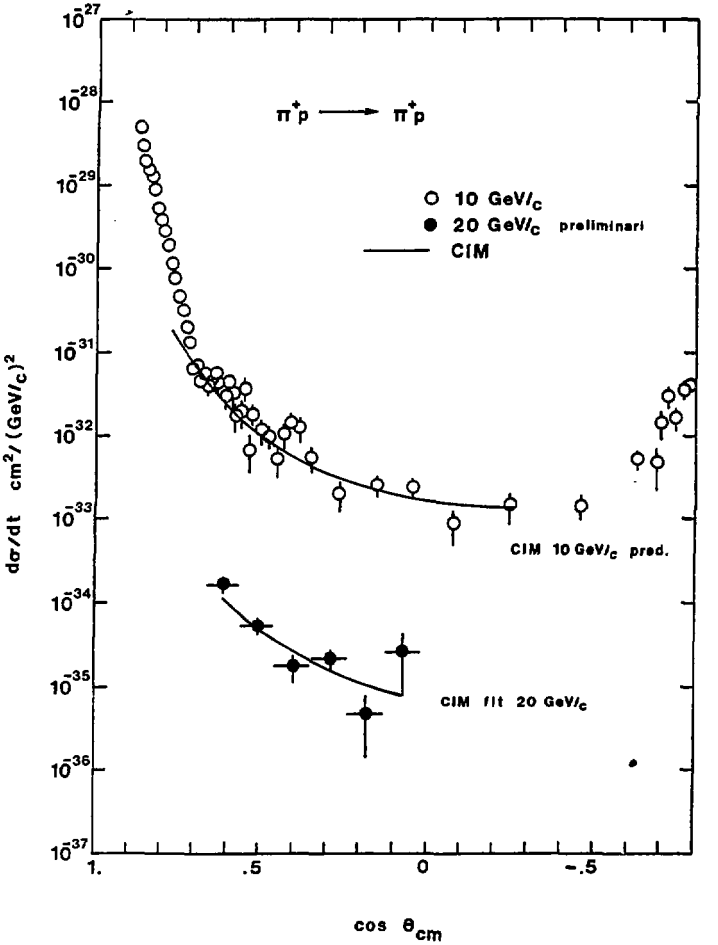
$\pi^+p \longrightarrow \pi^+p$
10 GeV/c
20 GeV/c preliminari
CIM
CIM 10 GeV/c pred.
CIM fit 20 GeV/c
$d\sigma/dt$ cm^2/(GeV/c)^2
cos θ_{cm}
10^{-27}
10^{-28}
10^{-29}
10^{-30}
10^{-31}
10^{-32}
10^{-33}
10^{-34}
10^{-35}
10^{-36}
10^{-37}
1.
.5
0
-.5

Fig. 22

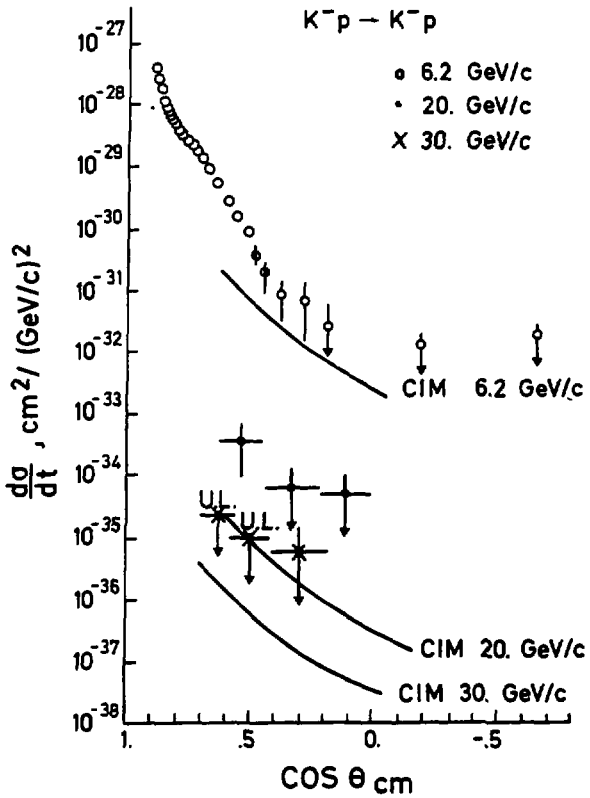
K⁻p → K⁻p
o 6.2 GeV/c
• 20. GeV/c
X 30. GeV/c
CIM 6.2 GeV/c
CIM 20. GeV/c
CIM 30. GeV/c
UL.
UL.
dσ/dt , cm²/ (GeV/c)²
10⁻²⁷
10⁻²⁸
10⁻²⁹
10⁻³⁰
10⁻³¹
10⁻³²
10⁻³³
10⁻³⁴
10⁻³⁵
10⁻³⁶
10⁻³⁷
10⁻³⁸
1.
.5
0.
-.5
COS θ cm

Fig. 23

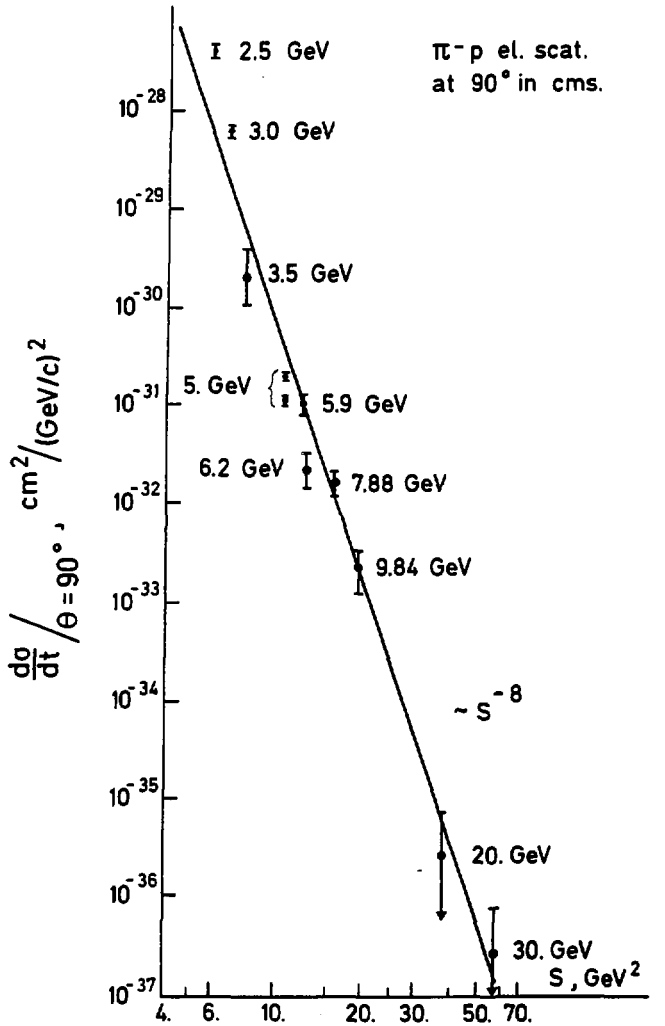
I 2.5 GeV
π⁻p el. scat.
at 90° in cms.
I 3.0 GeV
3.5 GeV
5. GeV
5.9 GeV
6.2 GeV
7.88 GeV
9.84 GeV
~ S⁻⁸
20. GeV
30. GeV
S, GeV²
dσ/dt /θ=90°, cm²/(GeV/c)²
10⁻²⁸
10⁻²⁹
10⁻³⁰
10⁻³¹
10⁻³²
10⁻³³
10⁻³⁴
10⁻³⁵
10⁻³⁶
10⁻³⁷
4.
6.
10.
20.
30.
50.
70.

Fig. 24

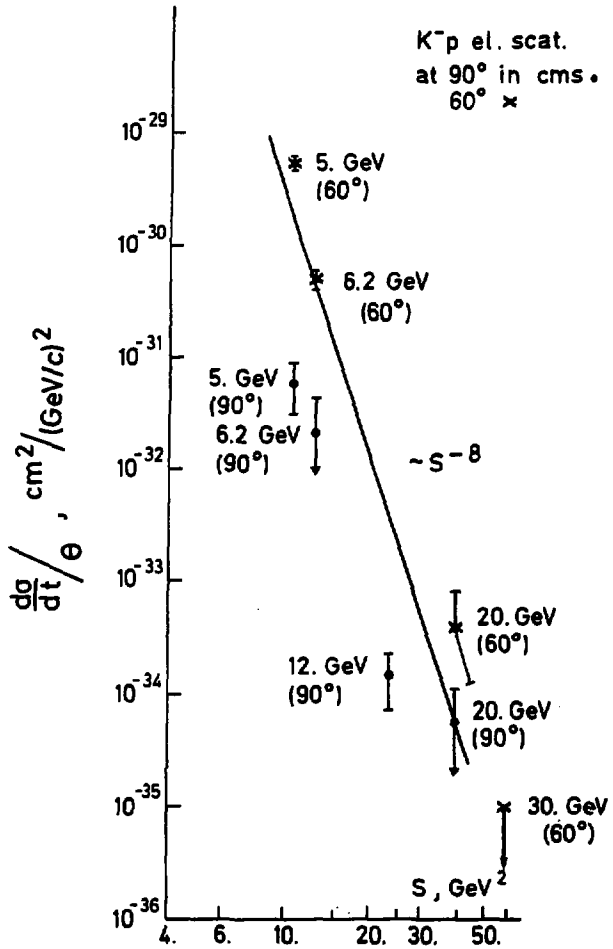
K⁻p el. scat.
at 90° in cms.
60° ×
5. GeV
(60°)
6.2 GeV
(60°)
5. GeV
(90°)
6.2 GeV
(90°)
~S⁻⁸
20. GeV
(60°)
12. GeV
(90°)
20. GeV
(90°)
30. GeV
(60°)
S , GeV²
dσ/dt/θ , cm²/(GeV/c)²
10⁻²⁹
10⁻³⁰
10⁻³¹
10⁻³²
10⁻³³
10⁻³⁴
10⁻³⁵
10⁻³⁶
4.
6.
10.
20.
30.
50.

Fig. 25

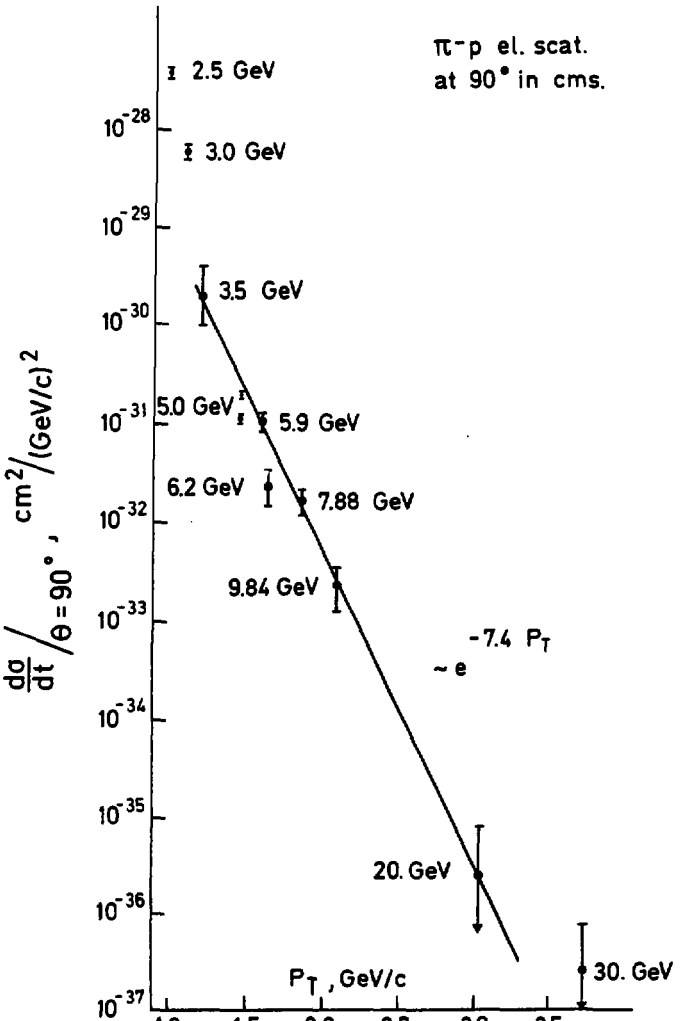
π⁻p el. scat.
at 90° in cms.
2.5 GeV
3.0 GeV
3.5 GeV
5.0 GeV
5.9 GeV
6.2 GeV
7.88 GeV
9.84 GeV
20. GeV
30. GeV
~ e^-7.4 P_T
dσ/dt /θ=90°, cm²/(GeV/c)²
P_T, GeV/c
10^-28
10^-29
10^-30
10^-31
10^-32
10^-33
10^-34
10^-35
10^-36
10^-37
1.0
1.5
2.0
2.5
3.0
3.5

Fig. 26

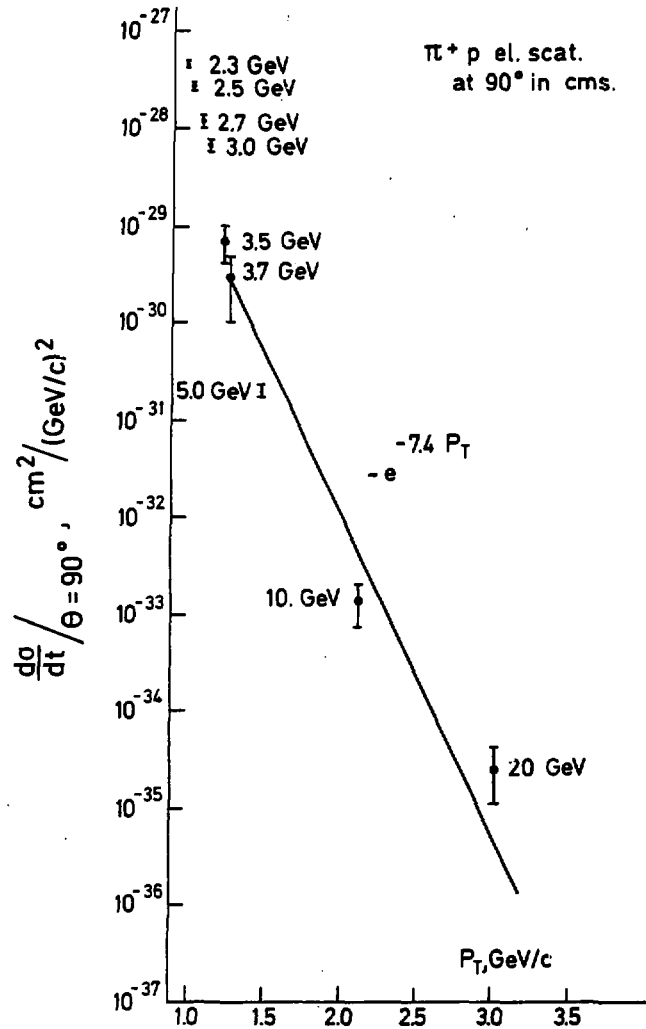
π^+ p el. scat.
at 90° in cms.
2.3 GeV
2.5 GeV
2.7 GeV
3.0 GeV
3.5 GeV
3.7 GeV
5.0 GeV
-7.4 P_T
- e
10. GeV
20 GeV
P_T,GeV/c
$\frac{d\sigma}{dt}/\theta=90°$, $cm^2/(GeV/c)^2$
10^{-27}
10^{-28}
10^{-29}
10^{-30}
10^{-31}
10^{-32}
10^{-33}
10^{-34}
10^{-35}
10^{-36}
10^{-37}
1.0
1.5
2.0
2.5
3.0
3.5

Fig. 27

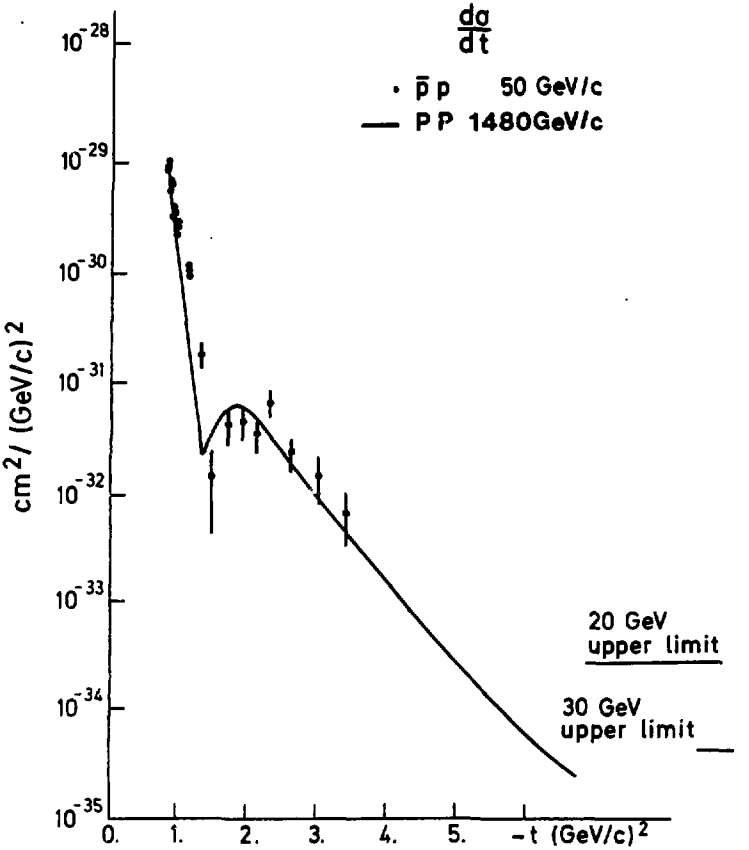
dσ/dt
• p̄ p 50 GeV/c
— P P 1480GeV/c
10^-28
10^-29
10^-30
10^-31
10^-32
10^-33
10^-34
10^-35
cm^2/ (GeV/c)^2
0.
1.
2.
3.
4.
5.
-t (GeV/c)^2
20 GeV
upper limit
30 GeV
upper limit

Fig. 28

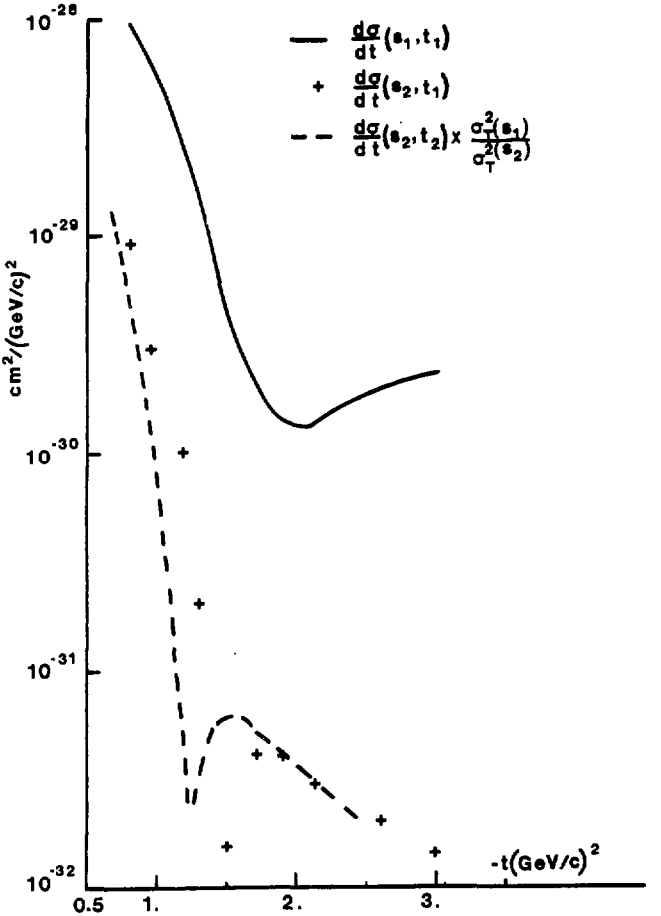
10^{-28}
10^{-29}
10^{-30}
10^{-31}
10^{-32}
$cm^2/(GeV/c)^2$
$\frac{d\sigma}{dt}(s_1,t_1)$
$\frac{d\sigma}{dt}(s_2,t_1)$
$\frac{d\sigma}{dt}(s_2,t_2) \times \frac{\sigma_T^2(s_1)}{\sigma_T^2(s_2)}$
0.5
1.
2.
3.
$-t(GeV/c)^2$

Fig. 29

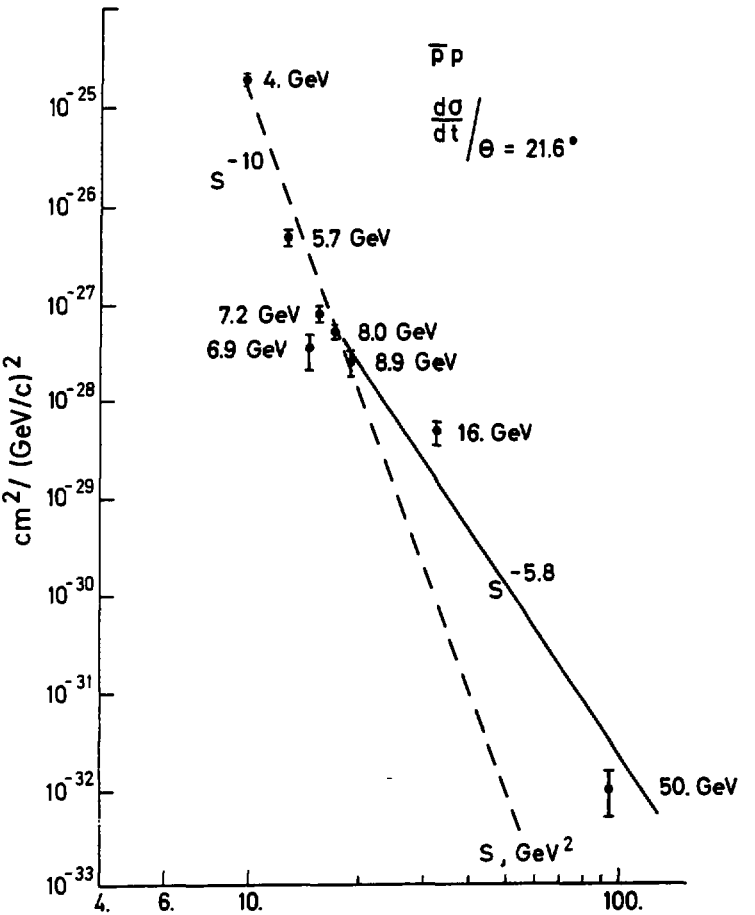
$\bar{p}p$
$\frac{d\sigma}{dt}/\theta = 21.6°$
4. GeV
5.7 GeV
7.2 GeV
6.9 GeV
8.0 GeV
8.9 GeV
16. GeV
50. GeV
S^{-10}
$S^{-5.8}$
$cm^2/(GeV/c)^2$
10^{-25}
10^{-26}
10^{-27}
10^{-28}
10^{-29}
10^{-30}
10^{-31}
10^{-32}
10^{-33}
4.
6.
10.
100.
S, GeV^2

Fig. 30

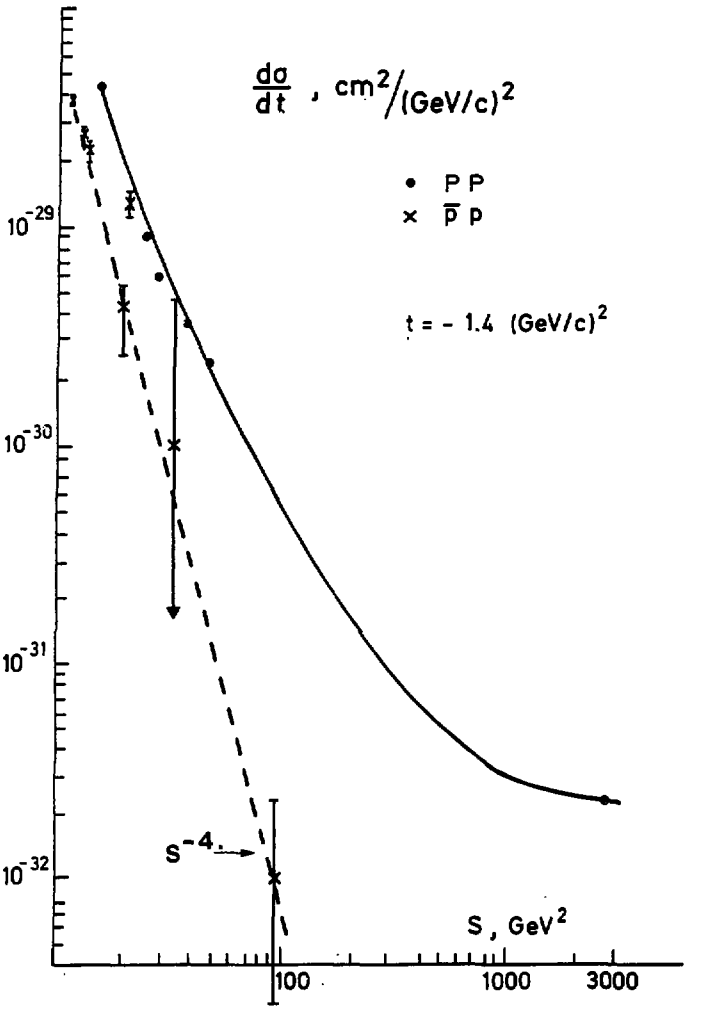
dσ/dt , cm²/(GeV/c)²
• P P
× p̄ p
t = - 1.4 (GeV/c)²
10⁻²⁹
10⁻³⁰
10⁻³¹
10⁻³²
S⁻⁴.
S , GeV²
100
1000
3000

Fig. 31

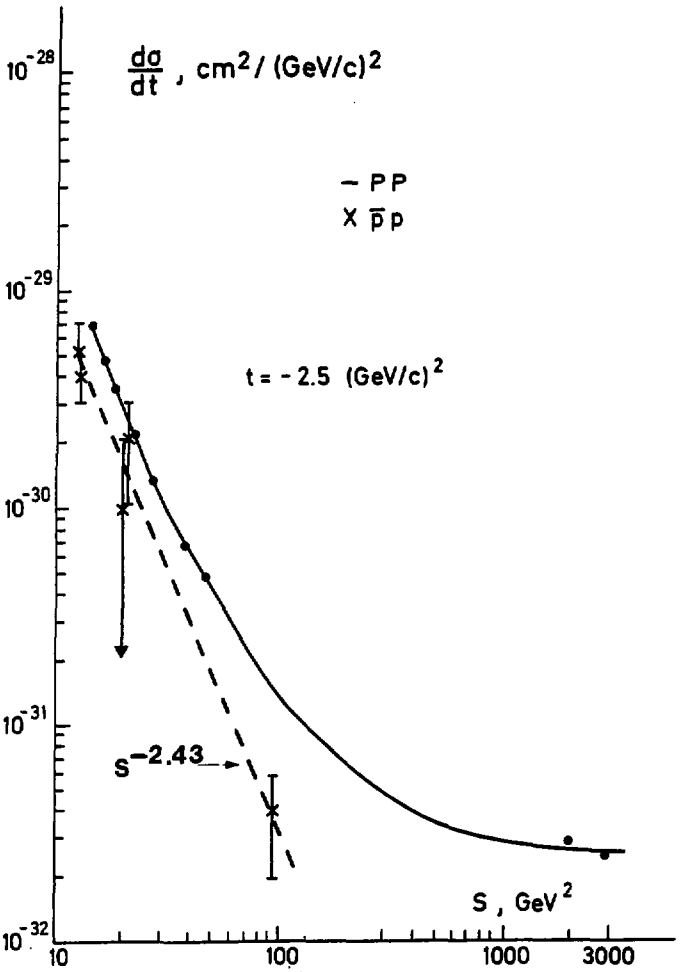
$\frac{d\sigma}{dt}$, cm^2/ (GeV/c)^2
10^{-28}
10^{-29}
10^{-30}
10^{-31}
10^{-32}
– P P
X $\bar{p}$ p
t = - 2.5 (GeV/c)^2
s$^{-2.43}$
S , GeV^2
10
100
1000
3000

Fig. 32

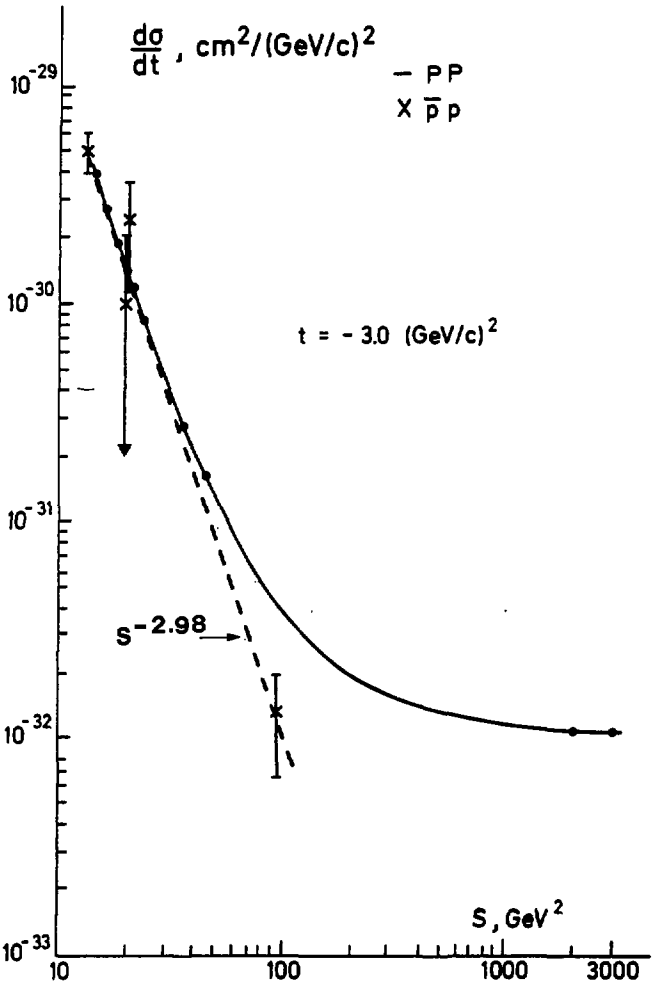
dσ/dt , cm²/(GeV/c)²
— P P
X p̄ p
t = - 3.0 (GeV/c)²
S^-2.98
S, GeV²
10^-29
10^-30
10^-31
10^-32
10^-33
10
100
1000
3000

Fig.33